

# Planetary nebulae in M33: probes of AGB nucleosynthesis and ISM abundances<sup>\*</sup>

F. Bresolin,<sup>1†</sup> G. Stasińska,<sup>2</sup> J.M. Vílchez,<sup>3</sup> J.D. Simon,<sup>4</sup> and E. Rosolowsky<sup>5</sup>

<sup>1</sup>*Institute for Astronomy, 2680 Woodlawn Drive, Honolulu, HI 96822, USA*

<sup>2</sup>*LUTH, Observatoire de Paris, CNRS, Université Paris Diderot, Place Jules Janssen, 92190 Meudon, France*

<sup>3</sup>*Instituto de Astrofísica de Andalucía (CSIC), Apartado 3004, 18080 Granada, Spain*

<sup>4</sup>*Observatories of the Carnegie Institution of Washington, Pasadena, CA 91101, USA*

<sup>5</sup>*University of British Columbia, Okanagan, 3333 University Way, Kelowna BC V1V 1V7, Canada*

6 June 2018

## ABSTRACT

We have obtained deep optical spectrophotometry of 16 planetary nebulae in M33, mostly located in the central two kpc of the galaxy, with the Subaru and Keck telescopes. We have derived electron temperatures and chemical abundances from the detection of the [O III]  $\lambda$ 4363 line for the whole sample. We have found one object with an extreme nitrogen abundance,  $12+\log(\text{N}/\text{H})=9.20$ , accompanied by a large helium content. After combining our data with those available in the literature for PNe and H II regions, we have examined the behavior of nitrogen, neon, oxygen and argon in relation to each other, and as a function of galactocentric distance. We confirm the good correlation between Ne/H and O/H for PNe in M33. Ar/H is also found to correlate with O/H. This strengthens the idea that at the metallicity of the bright PNe analyzed in M33, which is similar to that found in the LMC, these elements have not been significantly modified during the dredge-up processes that take place during the AGB phase of their progenitor stars. We find no significant oxygen abundance offset between PNe and H II regions at any given galactocentric distance, despite the fact that these objects represent different age groups in the evolution of the galaxy. Combining the results from PNe and H II regions, we obtain a representative slope of the ISM  $\alpha$ -element (O, Ar, Ne) abundance gradient in M33 of  $-0.025 \pm 0.006 \text{ dex kpc}^{-1}$ . Both PNe and H II regions display a large abundance dispersion at any given distance from the galactic center. We find that the N/O ratio in PNe is enhanced, relative to the H II regions, by approximately 0.8 dex.

**Key words:** galaxies: abundances – galaxies: ISM – planetary nebulae – galaxies: individual: M33.

## 1 INTRODUCTION

Planetary nebulae (PNe) can be used as test particles in the study of the chemical enrichment of galaxies and as fossil records of the nucleosynthesis that took place in previous generations of stars. While information on present-day chemical abundances of star-forming galaxies are gathered from the spectra of H II regions and massive stars, PNe pro-

vide the chemical makeup of older progenitor stars. Moreover, imprinted on their emission-line spectra are the signatures of chemical elements synthesized during the AGB phase of low- and intermediate-mass stars. Various processes occurring in these stars, such as third dredge-up and hot bottom burning, can strongly modify the helium, nitrogen and carbon abundances of the outer layers, which are eventually blown out to form the observed PNe. The effects on other elements, such as oxygen and neon, can be more subtle, and are currently the subject of lively debate (Stasińska 2008; Cristallo et al. 2009).

PNe represent an alternative to H II regions in the measurement of galactic abundance gradients, allowing tests of the evolution predicted by models of galaxy assembly (e.g. in the context of an inside-out formation, Prantzos & Boissier 2000). In addition, PNe can be used to test H II region abundances in cases where the latter are expected by theoretic-

<sup>\*</sup> Based on data collected at the Subaru Telescope, which is operated by the National Astronomical Observatory of Japan, and at the W.M. Keck Observatory, which is operated as a scientific partnership among the California Institute of Technology, the University of California and the National Aeronautics and Space Administration. The Observatory was made possible by the generous financial support of the W.M. Keck Foundation.

† E-mail: bresolin@ifa.hawaii.edu

cal calculations to be affected by systematic errors. These tests are particularly important in the central, metal-rich regions of spiral galaxies, where the high metal content could lead to systematic underestimates of the nebular metallicity (Stasińska 2005). This originally motivated our new investigation of a sample of luminous PNe in the central region of the galaxy M33. Despite the faintness of the targets in this external galaxy, compared to objects in the Milky Way, the uncertainty on the relative galactocentric distances, that afflicts studies in the Galaxy, is virtually removed. This offers a clear advantage in the determination of abundance gradients, and consequently in deriving information on the chemical evolution of the host galaxy, as well as providing empirical constraints on the metallicity dependence of extragalactic distance indicators (e.g., the Cepheid period-luminosity relation: Kennicutt et al. 1998, Scowcroft et al. 2009).

In this paper we present new spectroscopic observations of 16 PNe in the neighboring galaxy M33, obtained with the aim of measuring chemical abundances from the [O III]  $\lambda$ 4363 diagnostic line in the central few kpc of this galaxy. This classical ‘direct’ method is reckoned to yield the most accurate nebular abundances, unaffected by systematic uncertainties and/or strong-line method calibration issues, although in extragalactic PN and H II region work its application is made difficult, especially at high metallicity or large redshift, by the weakness of the  $\lambda$ 4363 auroral line. Combining our new data with existing observations in the literature we discuss the abundances of He, O, Ne, N and Ar in relation to each other, and as a function of galactocentric distance, in order to provide a clearer picture of the chemical composition and evolution of M33. The number of recent studies on the present-day chemical composition of ionized nebulae (Crockett et al. 2006; Rosolowsky & Simon 2008; Magrini, Stanghellini, & Villaver 2009) and massive stars (U et al. 2009) in M33 attests to the key role played by this Milky Way neighbour in the investigation of the chemical evolution of spiral galaxies.

## 2 OBSERVATIONS AND DATA REDUCTION

Deep multi-slit spectra of PNe in the central region of M33 were obtained at the 8.2m Subaru Telescope equipped with the Faint Object Camera and Spectrograph (FOCAS, Kashikawa et al. 2002) on 2007 October 9–10. Narrow-band [O III]  $\lambda$ 5007 images obtained with the same instrument were used, together with the PNe coordinates from Magrini et al. (2001) and Ciardullo et al. (2004), to select targets and prepare the multi-object masks in two circular fields of 3' radius. One of the fields contained the nucleus of the galaxy (the field center is approximately 1.5 arcmin SE of the galaxy center), while the second one was centered 7' to the N of the nucleus (coordinates of the field centers are given in Table 1).

For the spectroscopic observations we used 1''-wide slits and a combination of three different grisms (300R in second order, 300B and VPH650) to secure a continuous wavelength coverage from the near-UV (in most cases including the [O II]  $\lambda$ 3727 line) to the red (up to [Ar III]  $\lambda$ 7135), with a maximum spectral resolution of 4.5 Å (300R grism in the blue) and 4.0 Å (VPH650 grism in the red). Seeing con-

**Table 1.** Log of the observations (Subaru/FOCAS).

Field	R.A. Dec. (J2000)	Exposure time (s)	Grism
1	01 <sup>h</sup> 33 <sup>m</sup> 54 <sup>s</sup> .14 30°38'16''.5	3 × 1800	300R
		1 × 1200	300B
		2 × 1200	VPH650
2	01 <sup>h</sup> 34 <sup>m</sup> 03 <sup>s</sup> .61 30°45'43''.6	3 × 1800	300R
		1 × 900	300B
		3 × 1200	VPH650

ditions during the exposures presented here varied between 0.8 and 1.0 arcsec during the first night, and between 0.5 and 0.7 arcsec during the second night. Additional spectra were obtained in 2008 under worse atmospheric conditions (seeing up to 2 arcsec), but due to their poor quality they were not included in the analysis. The spectrophotometric standards G 191-B2B, GD 71 and LDS 749B were observed to flux calibrate the PNe spectra. Table 1 summarizes the exposure times used with the various grisms.

The data reduction was carried out by means of standard IRAF<sup>1</sup> tasks, and included bias and flat-field corrections, wavelength calibration from thorium-argon lamp exposures, cosmic-ray removal with the L.A.COSMIC routine (van Dokkum 2001), flux calibration and spectra co-addition. The subtraction of the background was carried out locally for each individual PN, from the flux measured within the corresponding slitlet, each of which was sufficiently long ( $\sim$ 20 arcsec) to allow a good sampling of the background (a linear fit to the background measured in the vicinity of each PN was sufficient). This step is crucial for the correct measurement of the low-excitation lines, which can be present in emission also in the diffuse ISM. It is worth pointing out in this context that in general the sky subtraction obtained from slit spectra is known to be superior to what can be achieved with fiber-fed spectrographs, being less prone to systematic errors.

PNe spectra were also obtained on 2004 September 22–23 and October 21 with the Keck I telescope and the Low-Resolution Imaging Spectrometer (LRIS, Oke et al. 1995) as part of the spectroscopic survey of H II regions in the southern half of M33 by Rosolowsky & Simon (2008). The Keck sample extends the galactocentric distance coverage of our sample to larger radii. The blue spectra presented here, extending from [O II]  $\lambda$ 3727 to [O III]  $\lambda$ 5007, were obtained with the 600/4000 grism, providing  $\sim$ 5 Å resolution with the 1''-wide slits used in the multi-object masks. More details on the reduction of the Keck dataset can be found in Rosolowsky & Simon (2008, = RS08).

For our chemical abundance analysis we retained only spectra for which we had a reliable detection of the  $T_e$ -sensitive line [O III]  $\lambda$ 4363. This left us with 10 and 8 PNe from the Subaru and the Keck observations, respectively, with two targets in common between the two datasets. Only

<sup>1</sup> IRAF is distributed by the National Optical Astronomy Observatory, which is operated by the Association of Universities for Research in Astronomy (AURA) under cooperative agreement with the National Science Foundation.

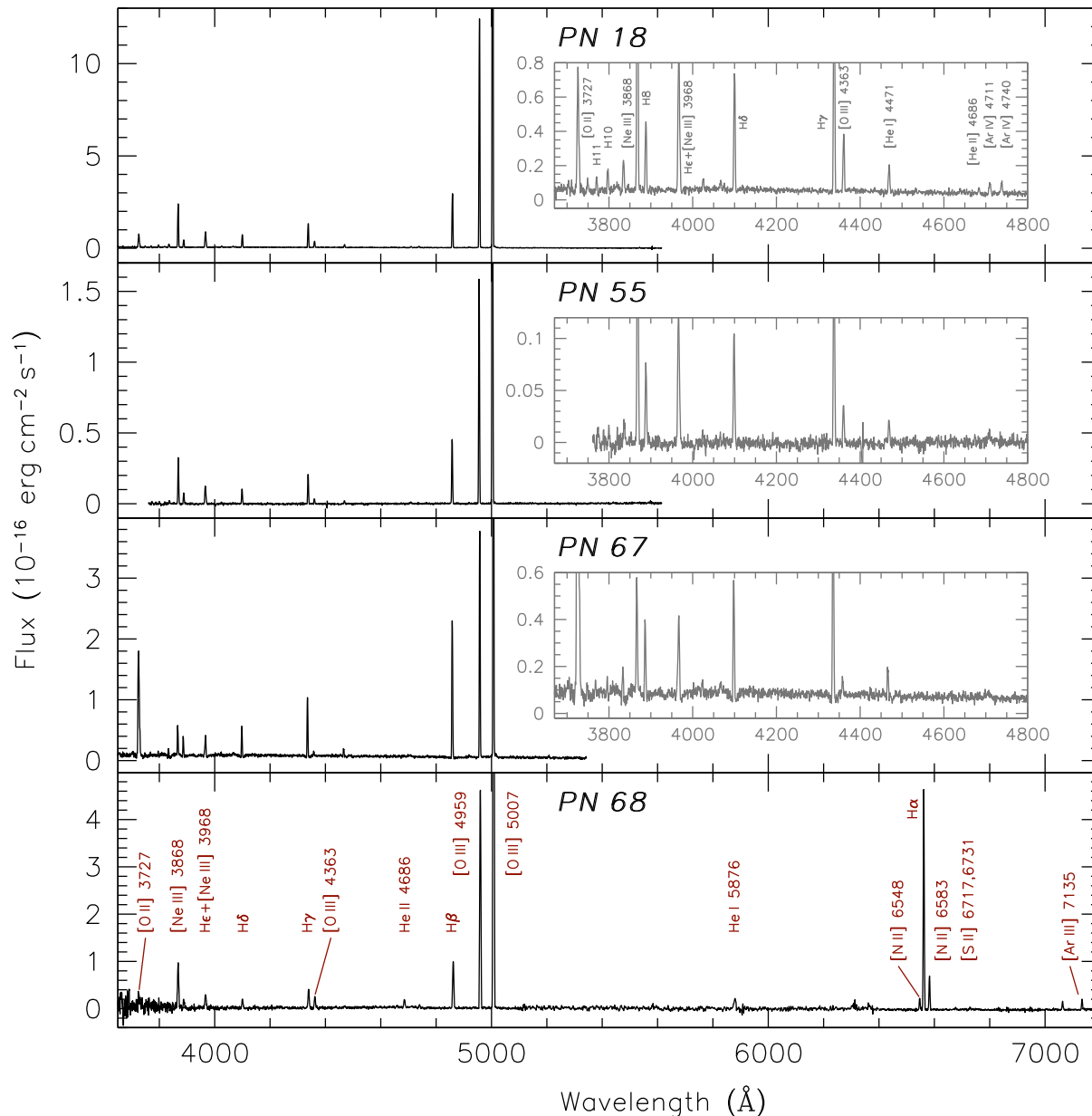


**Figure 1.** Spectra of PN 18, PN 55, PN 67 and PN 68. Zoomed-in views are provided in the insets to better display the weakest features. The main emission lines are identified.

two Subaru targets were excluded from the analysis, because their [O III]  $\lambda 4363$  line could not be measured. The Subaru slit masks also included a few H II regions. For three of them (B 90 in Field 1, B 72 and B 302 in Field 2; we adopt the H II region identification from Boulesteix et al. 1974) we had a good quality measurement of the electron temperature from the [O III]  $\lambda 4363$  auroral lines. For the comparison between PNe and H II region chemical abundances (Section 5) we retain these additional objects. For B 72 and B 302, to our knowledge, no previous direct abundance determinations exist in the literature.

Celestial coordinates and galactocentric distances for the final sample of PNe and H II regions are summarized in Table 2, where the PNe coordinates and identifications are taken from the catalog by Ciardullo et al. (2004). For the

calculation of the de-projected galactocentric distances we adopted a disk inclination angle  $i = 56^\circ$  and a position angle  $\theta = 23^\circ$ , as used by Ciardullo et al. (2004). The position of the galaxy nucleus was set at RA(J2000) =  $01^{\text{h}}33^{\text{m}}50^{\text{s}}.92$ , DEC(J2000) =  $30^\circ39'36''.8$  (Massey et al. 1996). For consistency with previous nebular abundance investigations, we adopted the Cepheid distance of 840 kpc by Freedman et al. (2001), even though more recent studies suggest considerably larger values (up to 968 kpc: Bonanos et al. 2006, U et al. 2009). In Fig. 1-4 we show the spectra of the 16 PNe included in this work. It can be seen that none of the targets has detectable WR-like features.

As Table 2 shows, our sample includes 5 PNe with galactocentric distance  $R \lesssim 1$  kpc, and 11 are within 2 kpc from the galactic center (the 3 H II regions observed by us also

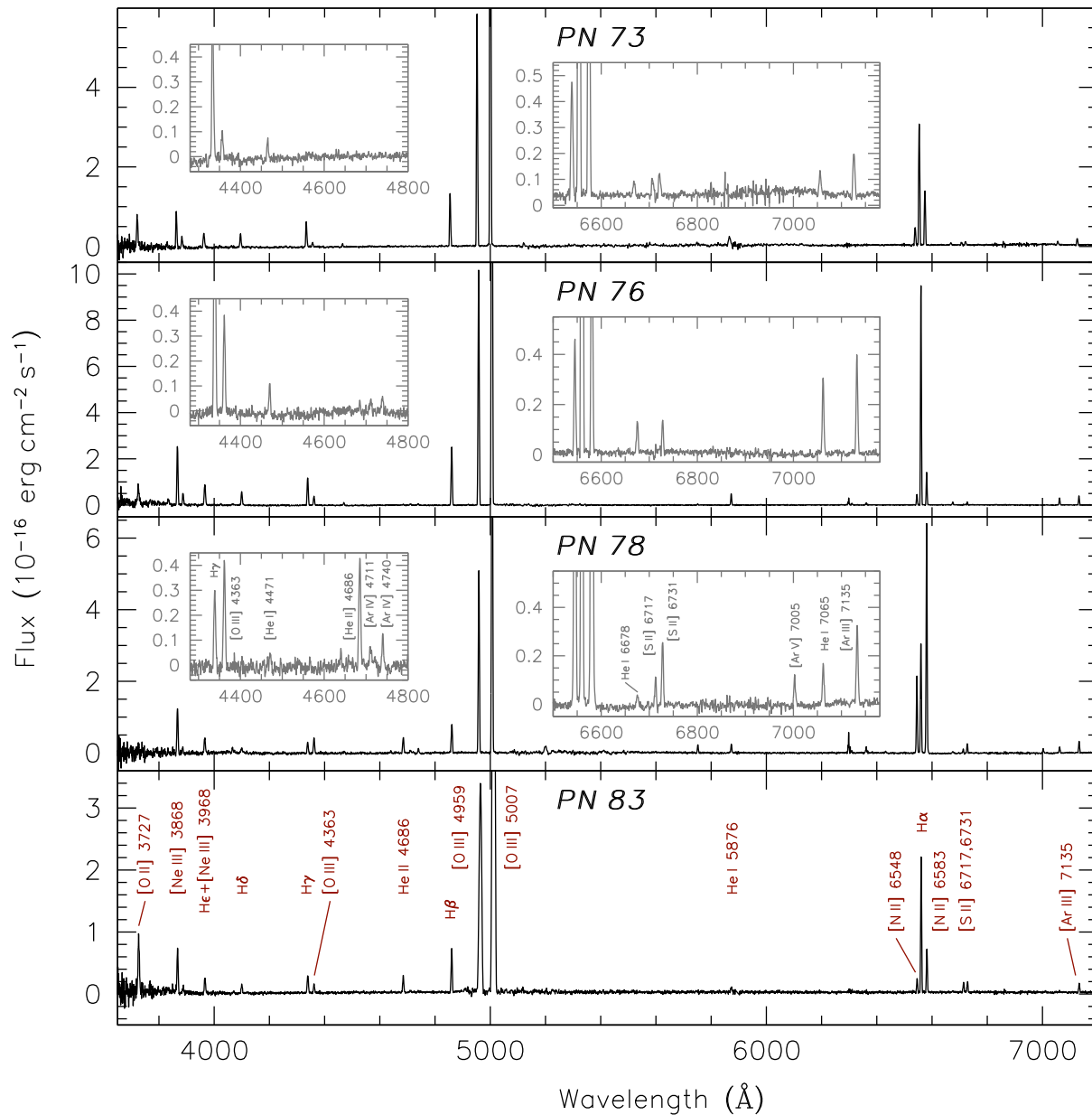


**Figure 2.** Spectra of PN 73, PN 76, PN 78 and PN 83. Zoomed-in views are provided in the insets to better display the weakest features. The main emission lines are identified.

lie in the central 2 kpc). This central region of the galaxy is under-represented in emission-line studies of the chemical composition of M33, because of the observational difficulties related to the measurement of the faint auroral lines in metal-rich environments. We also point out that the vast majority of the targets are expected to be part of the disk of M33. From the measurement of the kinematics of 140 PNe Ciardullo et al. (2004) determined that only two might belong to the halo of the galaxy, rather than the disk. One of them, PN 67, is included in our sample. Lastly, it is worth pointing out that the PNe observed as part of our program occupy the brightest 1.5  $m_{5007}$  magnitudes in the luminosity distribution of M33 planetaries.

The measurement of the emission line strengths was carried out with the `splot` program in IRAF. The extinc-

tion  $c(H\beta)$  was derived iteratively from the Balmer decrement, assuming case B H I line ratios (Hummer & Storey 1987) valid for the electron temperatures determined in Section 3. The reddening-corrected line fluxes, normalized to  $I(H\beta) = 100$ , and calculated using the Seaton (1979) interstellar reddening law, are presented in Tables 3 and 4. The extinction coefficient  $c(H\beta)$  appears in the last column of Table 2. The line flux errors account for the uncertainties in the placement of the continuum, in the flat fielding and the flux calibration, and in the extinction coefficient.

In two cases (PN 55 and 111) our spectra did not cover the bluest wavelengths, hence the entries for [O II]  $\lambda 3727$  and/or [Ne III]  $\lambda 3868$  are missing in Table 3. Similarly, the Keck spectra did not extend beyond [O III]  $\lambda 5007$ , therefore all the line fluxes at longer wavelengths are missing

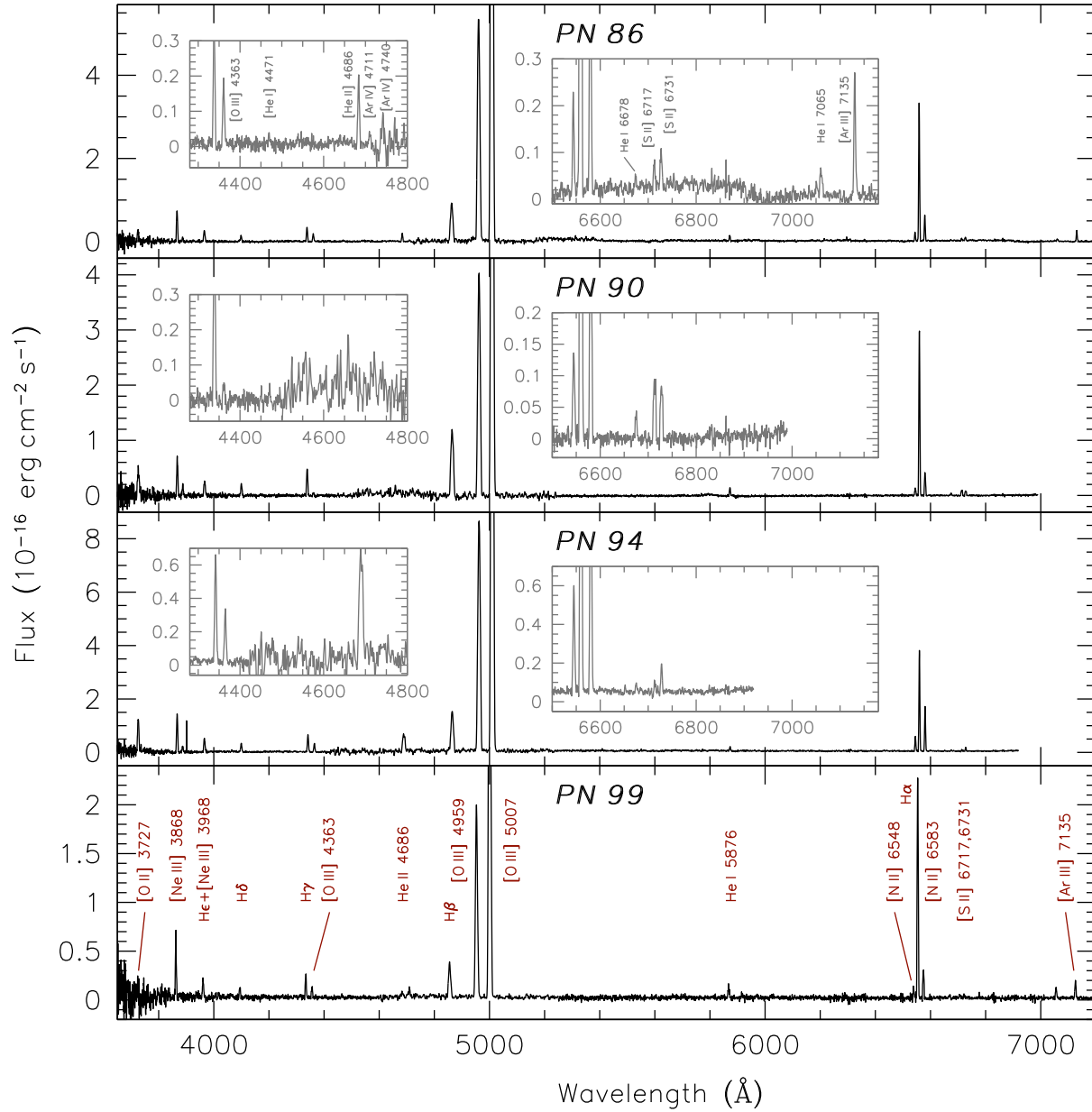


**Figure 3.** Spectra of PN 86, PN 90, PN 94 and PN 99. Zoomed-in views are provided in the insets to better display the weakest features. The main emission lines are identified.

for the corresponding targets in Table 4. In these tables we report the line fluxes measured independently from the Subaru/FOCAS and Keck/LRIS spectra for the two targets (PN 76 and PN 78) in common. This offers us a way to check the consistency of the flux intensities between the two samples, obtained from different instruments and reduced independently from each other. Considering the  $1-\sigma$  errors, we find quite a good agreement between the independent measurements.

We have compared our fluxes with those of Magrini et al. (2009, =M09) for the 11 PNe in common. The comparison is shown in Fig. 5, and it includes the O, Ne, N, S and Ar metal lines, as well as He I  $\lambda\lambda 4471, 5876$  and He II  $\lambda 4686$ . We show in colour the points representing O lines ([O II]  $\lambda 3727$ , [O III]  $\lambda 4363$  and [O III]  $\lambda 5007$ ), used

to derive the O abundance. The agreement is quite good for strong lines, and worsens with decreasing line strength. While most of the points lie within the 0.2 dex scatter region from the line of equality, there are several emission features that display a larger discrepancy. This is especially the case of the [S II]  $\lambda\lambda 6717, 6731$  lines, which are often quite faint in the spectra of PNe at the distance of M33, and which appear to be systematically too strong in the M09 sample compared to ours (open red squares in Fig. 5). A possible explanation is that the M09 spectra are affected by weak emission from the diffuse ionized gas (Haffner et al. 2009), which we clearly detect in our 2-D spectra and which might be not properly subtracted in the work by M09, who used fibers centered in low emission regions of the galaxy for the sky subtraction. The diffuse emission would be most

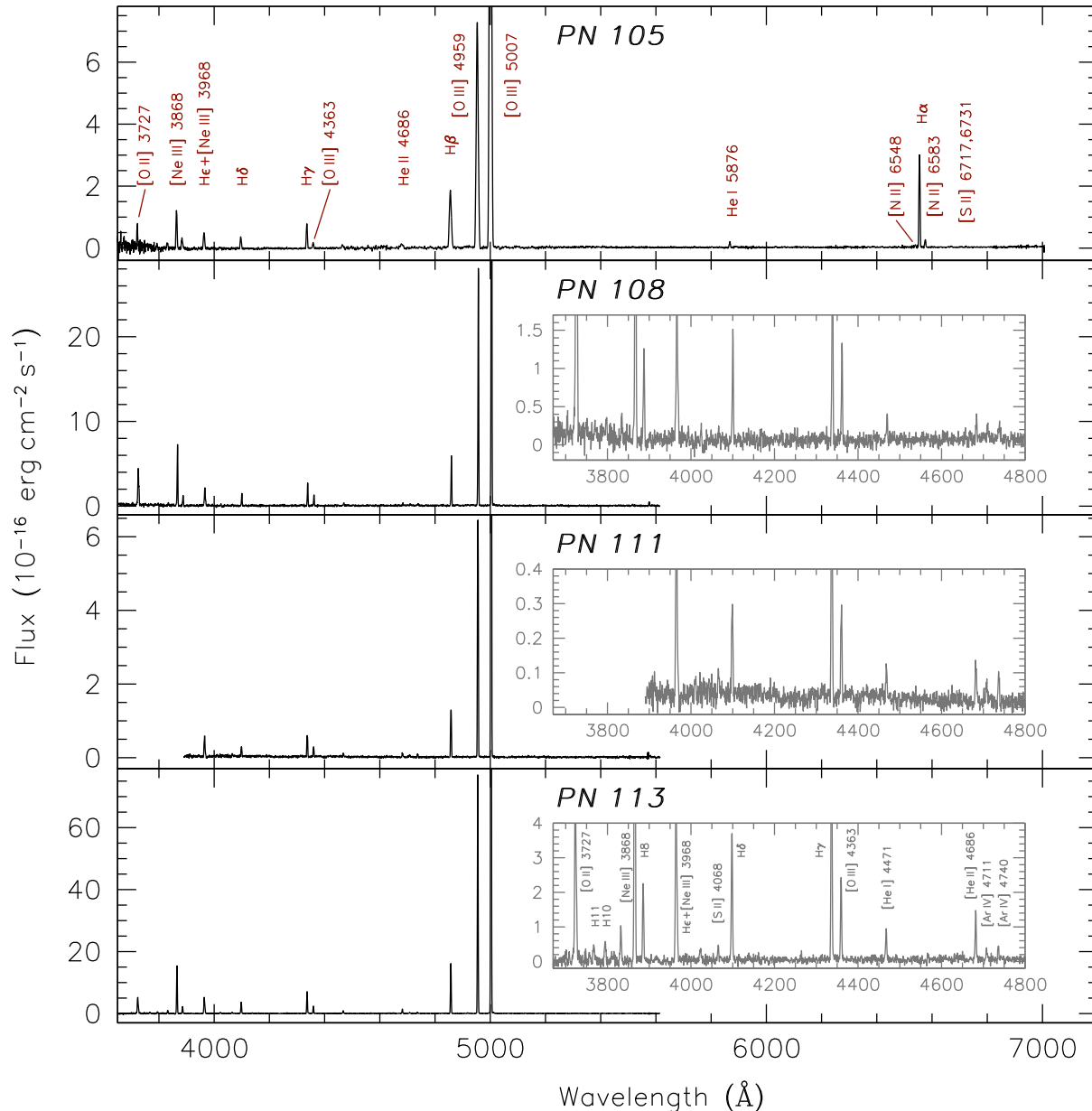


**Figure 4.** Spectra of PN 105, PN 108, PN 111 and PN 113. Zoomed-in views are provided in the insets to better display the weakest features. The main emission lines are identified..

important for faint, low-excitation metal lines, such as those of [S II], and the effects of an improper subtraction on the PN spectra would increase with decreasing line strength, as observed in Fig. 5.

We also found a large systematic difference concerning the extinction coefficient, our values being lower than those reported by M09 by an average factor of 2.5. We point out that our Balmer line intensity ratios agree with the theoretical values, while in several cases the  $H\gamma/H\beta$  and  $H\delta/H\beta$  ratios determined by M09 are significantly below the case B values. The means we derive from their data are  $0.403 \pm 0.102$  and  $0.220 \pm 0.057$ , respectively (case B values are 0.469 and 0.259 for  $T_e = 10^4$  K,  $N_e = 10^3$  cm $^{-3}$ ). This suggests a systematic over-estimate of the extinction coefficient.

The mean reddening for our PNe sample corresponds

to  $E(B - V) = 0.19 \pm 0.03$ . This is similar to other spectroscopic determinations of the reddening from studies of the young populations of M33, including H II regions (e.g. RS08:  $E(B - V) = 0.20 \pm 0.03$ ) and young stars (Massey et al. 1995:  $E(B - V) = 0.13 \pm 0.01$ ). The possibility that the PNe have reddening values that are much larger than those measured in young star-forming regions seems unlikely, even though a somewhat higher local reddening could be expected for PNe, since the progenitor AGB stars can produce dust shells.

### 3 CHEMICAL ABUNDANCES

For the derivation of the ionic abundances it is necessary to obtain the electron temperature  $T_e$  of the emitting gas. In principle, different excitation zones within the nebulae

**Table 2.** PNe and H II region sample.

Number	ID <sup>†</sup>	R.A. (J2000) <sup>†</sup> <i>h m s</i>	Dec. (J2000) <sup>†</sup> <i>° ' "</i>	$R^{\ddagger}$ (kpc)	Telescope*	$c(H\beta)$
PNe						
1.....	PN 18	01 33 06.11	30 31 04.5	3.73	K	0.33 ± 0.08
2.....	PN 55	01 33 40.16	30 37 49.5	0.88	K	0.12 ± 0.09
3.....	PN 67	01 33 48.27	30 33 15.7	1.71	K	0.37 ± 0.09
4.....	PN 68	01 33 48.57	30 35 47.9	1.01	S	0.50 ± 0.13
5.....	PN 73	01 33 51.06	30 45 38.8	1.70	S	0.00 ± 0.09
6.....	PN 76	01 33 52.77	30 37 38.9	0.64	S,K	0.03 ± 0.08
7.....	PN 78	01 33 54.68	30 36 05.7	1.17	S,K	0.27 ± 0.14
8.....	PN 83	01 33 57.18	30 36 47.6	1.14	S	0.02 ± 0.11
9.....	PN 86	01 33 59.97	30 40 28.7	0.74	S	0.31 ± 0.10
10.....	PN 90	01 34 02.57	30 40 00.5	1.00	S	0.16 ± 0.09
11.....	PN 94	01 34 03.54	30 39 15.6	1.17	S	0.05 ± 0.09
12.....	PN 99	01 34 06.56	30 48 23.3	2.30	S	0.47 ± 0.13
13.....	PN 105	01 34 11.91	30 45 00.9	1.87	S	0.00 ± 0.09
14.....	PN 108	01 34 13.40	30 33 50.7	3.05	K	0.15 ± 0.12
15.....	PN 111	01 34 14.79	30 31 49.6	3.62	K	0.22 ± 0.10
16.....	PN 113	01 34 15.48	30 32 20.3	3.55	K	0.28 ± 0.08
H II regions						
17.....	B 90	01 34 04.34	30 38 12.9	1.40	S	0.22 ± 0.07
18.....	B 302	01 34 06.92	30 47 26.1	2.09	S	0.25 ± 0.08
19.....	B 72	01 34 01.21	30 43 56.8	1.20	S	0.30 ± 0.07

<sup>†</sup>PNe coordinates from Ciardullo et al. (2004). H II region IDs are from Boulesteix et al. (1974), with positions determined from our images.

<sup>‡</sup>Galactocentric distance for  $D = 840$  kpc (Freedman et al. 2001).

\*S=Subaru, K=Keck.

**Table 3.** Reddening-corrected fluxes (blue).

ID	[O II] 3727	[Ne III] 3868	H $\delta$ 4101	H $\gamma$ 4340	[O III] 4363	He I 4471	He II 4686	[Ar IV] 4711	[Ar IV] 4740
PN 18	36 ± 3	91 ± 6	26 ± 2	47 ± 3	12.2 ± 0.8	6.0 ± 3.4	1.1 ± 0.3	2.8 ± 0.3	2.6 ± 0.3
PN 55	...	73 ± 5	25 ± 2	47 ± 3	8.5 ± 0.8	5.1 ± 0.8	(2.4)	(2.4)	(2.4)
PN 67	145 ± 10	24 ± 2	25 ± 2	47 ± 3	3.6 ± 0.5	5.1 ± 0.7	(0.5)	(0.5)	(0.5)
PN 68	43 ± 8	125 ± 9	23 ± 2	47 ± 3	26.9 ± 2.1	(4.0)	18.9 ± 1.4	(2.6)	5.2 ± 0.3
PN 73	71 ± 7	66 ± 5	27 ± 2	48 ± 3	8.8 ± 0.9	5.4 ± 0.6	(1.5)	(1.5)	(15.5)
PN 76 <sup>†</sup>	48 ± 4	101 ± 6	25 ± 2	47 ± 3	14.3 ± 0.9	5.0 ± 0.4	1.3 ± 0.3	2.1 ± 0.3	2.5 ± 0.3
PN 76 <sup>‡</sup>	41 ± 3	86 ± 6	24 ± 2	47 ± 3	13.3 ± 1.1	4.6 ± 1.8	2.0 ± 0.5	2.8 ± 0.5	3.0 ± 0.5
PN 78 <sup>†</sup>	24 ± 14	184 ± 13	26 ± 3	47 ± 3	58.7 ± 4.0	8.8 ± 1.7	58.7 ± 3.7	13.3 ± 1.7	14.8 ± 1.7
PN 78 <sup>‡</sup>	25 ± 4	170 ± 12	27 ± 3	47 ± 3	59.3 ± 4.0	7.3 ± 1.8	62.9 ± 4.2	13.3 ± 1.7	15.9 ± 1.7
PN 83	171 ± 15	104 ± 7	22 ± 2	47 ± 3	20.7 ± 1.8	(3.8)	38.7 ± 2.4	4.9 ± 0.8	3.8 ± 0.7
PN 86	47 ± 10	113 ± 8	26 ± 2	47 ± 3	26.2 ± 2.0	3.7 ± 1.2	24.1 ± 1.6	(2.2)	(3.5)
PN 90	69 ± 6	68 ± 5	23 ± 2	47 ± 3	8.0 ± 0.8	5.6 ± 0.9	(2.7)	(2.7)	(2.7)
PN 94	113 ± 9	105 ± 7	25 ± 2	47 ± 3	22.8 ± 1.5	(3.4)	35.4 ± 2.3	(3.2)	(3.2)
PN 99	35 ± 18	130 ± 9	27 ± 3	47 ± 3	22.9 ± 2.1	7.0 ± 1.6	10.6 ± 1.3	(3.2)	6.8 ± 1.1
PN 105	33 ± 5	76 ± 5	25 ± 2	47 ± 3	10.9 ± 0.9	(1.5)	8.3 ± 0.7	(1.5)	(1.5)
PN 108	117 ± 9	130 ± 9	26 ± 2	47 ± 3	22.3 ± 1.9	5.8 ± 1.2	5.3 ± 1.2	3.1 ± 1.1	3.4 ± 1.1
PN 111	...	...	23 ± 2	47 ± 3	20.0 ± 1.7	6.4 ± 1.2	9.7 ± 1.2	6.2 ± 1.2	6.4 ± 1.2
PN 113	53 ± 4	109 ± 8	27 ± 2	47 ± 3	15.5 ± 1.1	6.0 ± 0.6	8.3 ± 0.7	2.2 ± 0.5	2.6 ± 0.5
B 72	187 ± 12	5.8 ± 0.4	23 ± 1	47 ± 3	0.39 ± 0.04	4.3 ± 0.3	(0.1)	0.3 ± 0.04	(0.1)
B 90	196 ± 12	71 ± 4	24 ± 1	47 ± 3	5.2 ± 0.4	6.7 ± 0.4	4.4 ± 0.3	(0.6)	(0.6)
B 302	155 ± 10	6.1 ± 0.4	21 ± 1	46 ± 3	0.52 ± 0.04	3.8 ± 0.2	(0.1)	0.3 ± 0.03	(0.1)

Values in brackets are upper limits.

<sup>†</sup>Subaru/FOCAS spectrum. <sup>‡</sup>Keck/LRIS spectrum.

**Table 4.** Reddening-corrected fluxes (red).

ID	[O III] 5007	He I 5876	H $\alpha$ 6563	[N II] 6583	He I 6678	[S II] 6717	[S II] 6731	[Ar III] 7135
PN 18	1208 $\pm$ 71	...	...	...	...	...	...	...
PN 55	1052 $\pm$ 62	...	...	...	...	...	...	...
PN 67	476 $\pm$ 28	...	...	...	...	...	...	...
PN 68	1246 $\pm$ 73	13.0 $\pm$ 1.6	276 $\pm$ 32	44 $\pm$ 5	2.6 $\pm$ 0.5	(2.0)	2.9 $\pm$ 0.7	12.7 $\pm$ 1.5
PN 73	1296 $\pm$ 76	16.7 $\pm$ 2.2	303 $\pm$ 39	138 $\pm$ 18	5.8 $\pm$ 0.9	6.7 $\pm$ 1.0	8.6 $\pm$ 1.2	16.5 $\pm$ 2.3
PN 76 <sup>†</sup>	1169 $\pm$ 68	15.2 $\pm$ 1.8	282 $\pm$ 33	41 $\pm$ 5	3.8 $\pm$ 0.5	1.8 $\pm$ 0.3	3.5 $\pm$ 0.4	11.7 $\pm$ 1.4
PN 76 <sup>‡</sup>	1186 $\pm$ 70	...	...	...	...	...	...	...
PN 78 <sup>†</sup>	1699 $\pm$ 102	22.4 $\pm$ 2.8	275 $\pm$ 34	573 $\pm$ 70	6.2 $\pm$ 1.0	15.1 $\pm$ 2.0	26.8 $\pm$ 3.4	28.3 $\pm$ 3.6
PN 78 <sup>‡</sup>	1881 $\pm$ 113	...	...	...	...	...	...	...
PN 83	1337 $\pm$ 79	14.4 $\pm$ 2.2	281 $\pm$ 33	94 $\pm$ 11	(3.1)	22.5 $\pm$ 2.9	23.0 $\pm$ 3.0	19.6 $\pm$ 2.5
PN 86	1734 $\pm$ 103	13.2 $\pm$ 1.9	288 $\pm$ 34	53 $\pm$ 6	(2.2)	4.4 $\pm$ 0.9	7.3 $\pm$ 1.1	21.0 $\pm$ 2.6
PN 90	943 $\pm$ 56	14.6 $\pm$ 1.8	286 $\pm$ 33	43 $\pm$ 5	4.2 $\pm$ 0.5	11.8 $\pm$ 1.4	10.3 $\pm$ 1.2	...
PN 94	1813 $\pm$ 107	12.4 $\pm$ 1.6	280 $\pm$ 33	128 $\pm$ 15	3.4 $\pm$ 0.7	8.2 $\pm$ 1.1	9.6 $\pm$ 1.2	...
PN 99	1593 $\pm$ 94	21.2 $\pm$ 2.8	330 $\pm$ 40	45 $\pm$ 6	5.8 $\pm$ 1.0	5.5 $\pm$ 1.0	5.9 $\pm$ 1.0	24.1 $\pm$ 3.1
PN 105	1157 $\pm$ 68	15.8 $\pm$ 2.0	279 $\pm$ 34	23 $\pm$ 3	4.1 $\pm$ 0.6	(1.2)	2.5 $\pm$ 0.5	...
PN 108	1390 $\pm$ 83	...	...	...	...	...	...	...
PN 111	1553 $\pm$ 92	...	...	...	...	...	...	...
PN 113	1418 $\pm$ 83	...	...	...	...	...	...	...
B 72	146 $\pm$ 9	12.6 $\pm$ 1.5	309 $\pm$ 38	49 $\pm$ 6	3.8 $\pm$ 0.5	18.7 $\pm$ 2.3	13.7 $\pm$ 1.7	10.5 $\pm$ 1.3
B 90	698 $\pm$ 41	14.3 $\pm$ 1.7	280 $\pm$ 33	42 $\pm$ 5	3.5 $\pm$ 0.4	34.2 $\pm$ 4.0	24.4 $\pm$ 2.9	...
B 302	182 $\pm$ 11	12.6 $\pm$ 1.5	275 $\pm$ 33	33 $\pm$ 4	3.5 $\pm$ 0.4	13.4 $\pm$ 1.6	10.2 $\pm$ 1.2	9.9 $\pm$ 1.2

Values in brackets are upper limits.

<sup>†</sup>Subaru/FOCAS spectrum. <sup>‡</sup>Keck/LRIS spectrum.

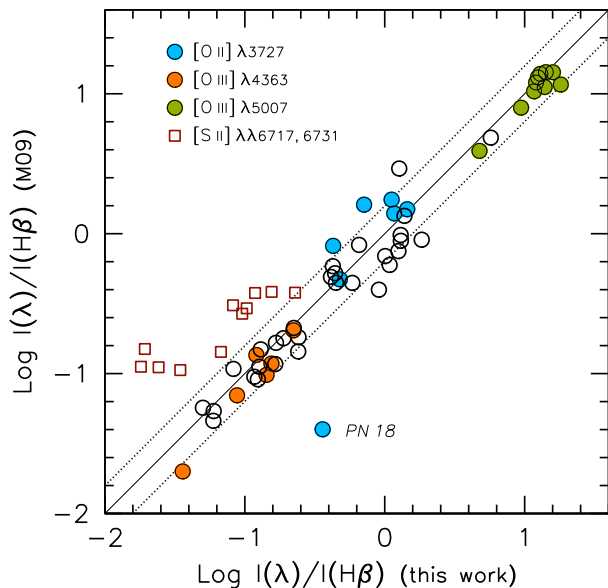


**Figure 5.** Comparison between the emission line fluxes of various spectral lines, relative to H $\beta$ , measured in this work and by Magrini et al. (2009), for 11 PNe in common. The line of one-to-one correspondence is flanked by lines drawn  $\pm 0.2$  dex from it. Points representing O lines are shown in colour: [O II]  $\lambda 3727$  (blue), [O III]  $\lambda 5007$  (green) and [O III]  $\lambda 4363$  (orange). The outlier [O II]  $\lambda 3727$  line for PN 18 is identified. The red open squares represent the [S II]  $\lambda\lambda 6717, 6731$  lines.

are characterized by different  $T_e$  values, that would require the detection of auroral lines of different ions, such as [O II]  $\lambda 7325$ , [S III]  $\lambda 6312$  and [O III]  $\lambda 4363$ . This is observationally quite challenging for PNe at the distance of

M33, and [O III]  $\lambda 4363$  is the only line that we are able to use to infer  $T_e$ , with the exception of two [N II]  $\lambda 5755$  detections (PN 76 and PN 78). Therefore, for the derivation of the ionic abundances we computed the line emissivities for all ions of interest at the electron temperature obtained from the [O III]  $\lambda 4363/(\lambda 4959 + \lambda 5007)$  line ratio. This includes the low-excitation line [O II]  $\lambda 3727$ , for which a different  $T_e$  might be appropriate, but since most of the oxygen in bright PNe is doubly ionized, this introduces a negligible error in the final O/H abundance. For PNe we did not use empirical temperature schemes between high- and low-excitation zones, since, for reasons yet not fully understood, the uncertainties would be large (see, for example, the behaviour of  $T_e$  derived from [N II]  $\lambda 5755/(\lambda 6548 + \lambda 6583)$  as a function of  $T_e$  from [O III]  $\lambda 4363/(\lambda 4959 + \lambda 5007)$  for a sample of Galactic PNe in Górný et al. 2009). For H II regions, however, we derived the temperature of the low-excitation zone (for the O<sup>+</sup> and N<sup>+</sup> ionic abundances) from the Garnett (1992) relation,  $T(\text{O}^+) = 0.7 T(\text{O}^{++}) + 3000$  K, which is supported by recent observations of extragalactic H II regions (Esteban et al. 2009; Bresolin et al. 2009).

The electron temperatures were derived using the five-level program *temden* (De Robertis, Dufour, & Hunt 1987), in the implementation of IRAF's *nebular* package (Shaw & Dufour 1995). The adopted atomic parameters are the same as in Bresolin et al. (2009), and are summarized in Table 5 for convenience. For He I we used the emissivities of Porter, Ferland, & MacAdam (2007), including the correction for collisional excitation, and for H I and He II those of Hummer & Storey (1987).

The electron densities were estimated from the [S II]  $\lambda 6717/\lambda 6731$  ratios, when available (Subaru data only), or from [Ar IV]  $\lambda 4711/\lambda 4740$ , if measured. We arbitrarily assumed  $N_e = 1000 \text{ cm}^{-3}$  in the remaining cases. The density

**Table 5.** Sources of atomic data.

Ion	Transition probabilities	Collision strengths
[O II]	Froese Fischer & Tachiev (2004)	Tayal (2007)
[O III]	Froese Fischer & Tachiev (2004)	Aggarwal & Keenan (1999)
[N II]	Froese Fischer & Tachiev (2004)	Hudson & Bell (2005)
[Ne III]	Froese Fischer & Tachiev (2004)	McLaughlin & Bell (2000)
[Ar III]	Mendoza (1983) Kaufman & Sugar (1986)	Galavis et al. (1995)
[S II]	Froese Fischer et al. (2006)	Ramsbottom et al. (1996)
[S III]	Froese Fischer et al. (2006)	Tayal & Gupta (1999)

affects the  $T_e$  determination only weakly, even though it has an important impact on the  $O^+$  emissivity. For example, around 12,000 K, a variation of  $N_e$  between  $1000 \text{ cm}^{-3}$  and  $5000 \text{ cm}^{-3}$  induces a change in  $T[\text{O III}]$  of 60 K, which is on the order of 10% of the estimated temperature errors. The emissivity of the [O II]  $\lambda 3727$  line changes by about 50%, but we have verified that this has little effect on our results. For the final  $T_e$  uncertainties (rounded to the nearest hundred K in Table 6) we have propagated the  $1\text{-}\sigma$  errors in the line fluxes (contained in Tables 3-4), and include the small contribution from the uncertainties in  $N_e$ . Table 6 summarizes the plasma diagnostics thus obtained, and the density values that we adopted. We note the generally good agreement between densities obtained from the [S II] and [Ar IV] line ratios, when both are available. In these cases (PN 76, PN 78 and PN 83) we have adopted the [S II]-based densities for the following analysis, because of their smaller uncertainties. Table 6 reports the plasma diagnostics for the two targets in common between the Subaru and Keck datasets (PN 76 and PN 78). Within the errors, we find a good agreement between independent determinations for both the  $T[\text{O III}]$  electron temperatures and the [Ar IV]-based electron densities.

The abundances of  $O^+$ ,  $O^{++}$ ,  $Ne^{++}$ ,  $N^+$ ,  $Ar^{++}$ ,  $He^+$  and  $He^{++}$ , relative to  $H^+$ , were derived with the *ionic* program in IRAF, from the de-reddened line fluxes and the  $T_e$ ,  $N_e$  values found in the previous step. Total chemical abundances were obtained adopting the ionization correction factors (ICFs) of Kingsburgh & Barlow (1994), with the exception of argon for the H II regions, in which case we adopted the recipes by Izotov et al. (2006). The ionization correction factor for oxygen is obtained as  $(1 + He^{2+}/He^+)^{2/3}$ , where the  $He^+$  abundance has been derived from  $He I \lambda 5876$  when available (Subaru dataset), and from  $He I \lambda 4471$  in the remaining cases. Our final abundances are shown in Table 7, where the uncertainties have been calculated by propagation of the errors in the line fluxes and  $T_e$ . Once again, we point out the good agreement in the resulting abundances between independent measurements for PN 76 and PN 78, observed both with Subaru and Keck. The weighted abundances for

these two PNe (also included in Table 7) will be adopted for the remainder of the paper.

For two of the Keck targets, PN 55 and PN 111, the  $O^+$  abundance could not be calculated, because the [O II]  $\lambda 3727$  line was outside the covered wavelength range, therefore the quoted value is a lower limit to the O/H ratio. However, the median  $O^+/O$  ratio of the remaining sample is 0.06, exceeding 0.12 only in the case of PN 67 (0.26), so the total oxygen abundance in PN 55 and PN 111 is likely to be close to the values reported in Table 7.

In Fig. 6 we compare our final PNe abundances with those obtained by M09. These authors have determined electron temperatures either from direct detections of auroral lines ([O III]  $\lambda 4363$ , [N II]  $\lambda 5755$ ), or from a statistical relationship between  $T_e$  and the strength of  $He II \lambda 4686$ . Abundances obtained with the latter method are not expected to be accurate, neither on theoretical grounds, nor on the basis of the diagrams by M09 which were used to define this relation. In order to differentiate the two  $T_e$ -determination methods, we represent the [O III]  $\lambda 4363$  detections in the M09 sample by full points in Fig. 6, while open symbols are used for PNe without a  $\lambda 4363$  line detection (we remind the reader that [O III]  $\lambda 4363$  is measured for each PN contained in our sample). It can be seen that the agreement between our abundances and those by M09 is generally acceptable, and that no obvious systematic offset exists between the two sets of abundances, with the exception of helium. This is likely a result of different abundance calculations, in particular regarding the effect of collisional excitation, because the  $He I$  line fluxes are in good agreement between the two studies. The remaining large discrepancies ( $> 0.2$  dex) in Fig. 6 are due to significant differences either in the measured diagnostic line strengths (as in the case of Ne), or in the adopted  $T_e$  (in the case of the most discrepant points for O, which do not have a [O III]  $\lambda 4363$ -based  $T_e$  determination in M09). The plot for O confirms the expectation that PNe in the M09 sample without an [O III]  $\lambda 4363$  detection, and whose abundances derive from a  $T_e$  determination based on  $He II \lambda 4686$ , are affected by larger random errors than those with an observed [O III]  $\lambda 4363$  line, and that a large abundance scatter is expected for these objects.

One of the three H II regions we observed, B 90, was also included in the abundance studies by Crockett et al. (2006) and RS08. Both obtained  $12 + \log(O/H) = 8.50 \pm 0.06$ , in very good agreement with our value  $12 + \log(O/H) = 8.47 \pm 0.08$ . The Ne/H abundance ratios are also virtually coincident.

For the remainder of the paper, we complement our dataset of 16 PNe, covering mostly the inner region of M33, with the PNe sample studied by M09, but considering only objects with a direct determination of the oxygen abundance, i.e. based on the measurement of the [O III]  $\lambda 4363$  auroral line. This restricts the number of PNe from M09 to 32 (out of 93), extending in galactocentric distances from 0.6 to 8 kpc. Of these, 6 are in common with our sample: PN 18, PN 67, PN 73, PN 76, PN 108, and PN 113. New auroral line-abundances for 10 PNe are therefore added by our study, 7 of them at  $R < 1.2$  kpc. For consistency, we have recalculated the chemical abundances from the line fluxes published by M09, with the same procedure used for our PNe sample. In the plots that follow, in the cases where

**Table 6.** Plasma diagnostics.

ID	T[O III]	T[N II]	$N_e$ ([S II])	$N_e$ ([Ar IV])	$N_e$ (adopted)
PN 18.....	11500 ± 500	...	...	3290 ± 820	3290 ± 820
PN 55.....	10700 ± 500	...	...	...	1000 ± 100
PN 67.....	10400 ± 600	...	...	...	1000 ± 100
PN 68.....	15700 ± 1000	...	...	...	1000 ± 100
PN 73.....	10100 ± 500	...	1060 ± 120	...	1060 ± 120
PN 76 <sup>†</sup> .....	12300 ± 600	13500 ± 3200	6020 ± 1420	8320 ± 1520	6020 ± 1420
PN 76 <sup>‡</sup> .....	11900 ± 600	...	...	6050 ± 1540	6050 ± 1540
PN 78 <sup>†</sup> .....	20100 ± 1600	14700 ± 2500	4910 ± 380	7680 ± 1210	4910 ± 380
PN 78 <sup>‡</sup> .....	18900 ± 1400	...	...	9360 ± 1310	9360 ± 1310
PN 83.....	13500 ± 800	...	540 ± 50	1100 ± 990	540 ± 50
PN 86.....	13400 ± 800	...	2980 ± 840	...	2980 ± 840
PN 90.....	10900 ± 600	...	240 ± 20	...	240 ± 20
PN 94.....	12500 ± 600	...	850 ± 80	...	850 ± 80
PN 99.....	13200 ± 800	...	660 ± 150	...	660 ± 150
PN 105.....	11200 ± 500	...	...	...	1000 ± 100
PN 108.....	13600 ± 900	...	...	6310 ± 3360	6310 ± 3360
PN 111.....	12500 ± 700	...	...	5230 ± 1530	5230 ± 1530
PN 113.....	11700 ± 600	...	...	7180 ± 2150	7180 ± 2150
B 72.....	7800 ± 300	...	51 ± 5	...	51 ± 5
B 90.....	10400 ± 400	10200 ± 1400	22 ± 2	...	22 ± 2
B 302.....	8000 ± 300	8100 ± 700	79 ± 8	...	79 ± 8

<sup>†</sup>Subaru/FOCAS spectrum. <sup>‡</sup>Keck/LRIS spectrum.

the M09 and our sample overlap, we have retained only the abundance information obtained from our observations, in order to avoid representing the same object more than once.

As mentioned above, Ciardullo et al. (2004) identified two PNe (PN 24 and PN 67) as possibly belonging to the M33 halo, having velocities that deviate more than  $2.5\sigma$  from the mean rotation curve. However, they point out that these outliers can be expected out of the total number of 140 targets, simply on statistical grounds. We find that the chemical abundances of PN 67 are comparable with those of the other targets in our sample. PNe in the halo of the Milky Way are generally metal-poor compared to those in the disk (e.g. Howard, Henry, & McCartney 1997; Henry, Kwitter, & Balick 2004). We conclude that PN 67 likely belongs to the disk of M33, rather than the halo. However, we also point out that PN 67 is the only object in our PN sample that clearly shows absorption components in the Balmer lines, an indication of the presence of an underlying stellar component, as in the case of H II regions. It has also the lowest excitation ratio observed in our sample,  $O^{++}/O = 0.74$ , which overlaps with the range observed for H II regions in M33 (however, PNe with even lower excitation are known, e.g. in the Milky Way, see Kingsburgh & Barlow 1994 or Górný et al. 2009). PN 67 is not among the brightest in  $H\alpha$  flux or in  $m_{5007}$  (Ciardullo et al. 2004). It is therefore unclear whether this is truly a PN, or a compact, high-excitation H II region. For the remainder of this paper we will continue to include PN 67 along the remaining PNe. None of the results presented in the next sections suggests that we should do otherwise.

#### 4 EXCITATION PROPERTIES

A first look at the main properties of the PNe in M33 is presented in Fig. 7, where we show the  $He^{++}/H$  and

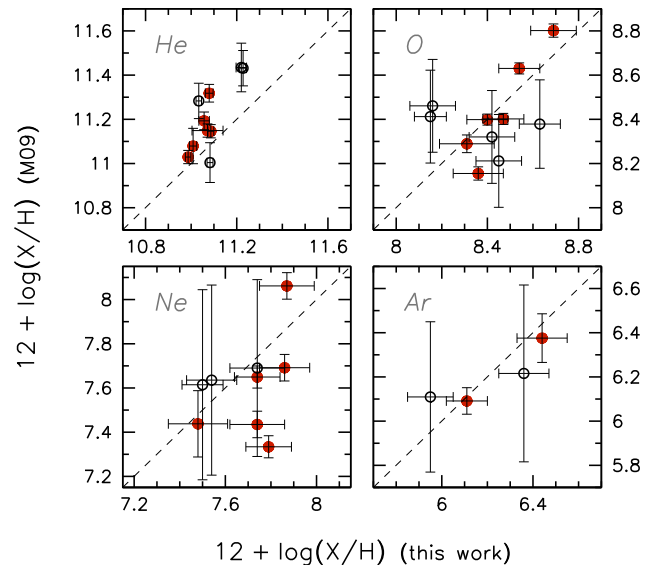


**Figure 6.** Comparison between the chemical abundances of He, O, Ne and Ar measured in this work and by Magrini et al. (2009, =M09) for PNe in common. Dashed lines are drawn to represent the one-to-one correspondence. Objects with an electron temperature determination based on [O III]  $\lambda 4363$  from the M09 sample are shown as red full dots.

N/O abundance ratios as a function of the excitation  $O^{++}/(O^+ + O^{++})$  (panels a and b). In this and subsequent plots we use red open circles to represent our new PN sample, while the green circles represent the PNe observed by M09 and with a [O III]  $\lambda 4363$  line detection. We also show with orange squares our new H II region abundances (B 72, B 90 and B 302), and with the remaining squares a sample of H II regions for which auroral line-based abundances could be derived, using line fluxes we compiled from the literature

**Table 7.** Chemical abundances.

ID	He/H	12 + log(O/H)	12 + log(N/H)	12 + log(Ne/H)	12 + log(Ar/H)
PN 18.....	0.12 ± 0.07	8.47 ± 0.09	...	7.79 ± 0.10	...
PN 55.....	0.10 ± 0.02	8.49* ± 0.10	...	7.79 ± 0.11	...
PN 67.....	0.10 ± 0.02	8.31 ± 0.12	...	7.48 ± 0.13	...
PN 68.....	0.11 ± 0.01	8.16 ± 0.10	8.07 ± 0.11	7.54 ± 0.11	5.95 ± 0.10
PN 73.....	0.12 ± 0.02	8.69 ± 0.10	8.62 ± 0.12	7.87 ± 0.12	6.44 ± 0.11
PN 76 <sup>†</sup> .....	0.10 ± 0.01	8.38 ± 0.09	7.89 ± 0.10	7.75 ± 0.10	6.11 ± 0.09
PN 76 <sup>‡</sup> .....	0.09 ± 0.04	8.43 ± 0.10	...	7.72 ± 0.11	...
PN 76 <sup>+</sup> .....	0.10 ± 0.01	8.40 ± 0.09	7.89 ± 0.10	7.74 ± 0.10	6.11 ± 0.09
PN 78 <sup>†</sup> .....	0.17 ± 0.02	8.11 ± 0.10	9.32 ± 0.11	7.48 ± 0.11	6.13 ± 0.11
PN 78 <sup>‡</sup> .....	0.18 ± 0.03	8.21 ± 0.10	...	7.51 ± 0.11	...
PN 78 <sup>+</sup> .....	0.17 ± 0.01	8.15 ± 0.07	9.32 ± 0.11	7.50 ± 0.09	6.13 ± 0.11
PN 83.....	0.14 ± 0.02	8.41 ± 0.10	8.01 ± 0.11	7.71 ± 0.11	6.25 ± 0.11
PN 86.....	0.11 ± 0.01	8.49 ± 0.10	8.27 ± 0.11	7.71 ± 0.11	6.29 ± 0.10
PN 90.....	0.11 ± 0.02	8.45 ± 0.10	7.99 ± 0.11	7.77 ± 0.12	...
PN 94.....	0.12 ± 0.01	8.63 ± 0.09	8.47 ± 0.10	7.81 ± 0.10	...
PN 99.....	0.17 ± 0.02	8.42 ± 0.10	8.36 ± 0.11	7.74 ± 0.12	6.36 ± 0.11
PN 105.....	0.12 ± 0.02	8.49 ± 0.09	8.04 ± 0.11	7.76 ± 0.11	...
PN 108.....	0.11 ± 0.02	8.36 ± 0.11	...	7.74 ± 0.12	...
PN 111.....	0.13 ± 0.02	8.47* ± 0.10	...	7.74 ± 0.12	...
PN 113.....	0.12 ± 0.01	8.54 ± 0.09	...	7.86 ± 0.11	...
B 72.....	0.09 ± 0.01	8.46 ± 0.09	7.45 ± 0.09	7.62 ± 0.12	6.31 ± 0.11
B 90.....	0.11 ± 0.01	8.47 ± 0.08	7.53 ± 0.08	7.94 ± 0.10	...
B 302.....	0.09 ± 0.01	8.44 ± 0.08	7.36 ± 0.08	7.52 ± 0.10	6.25 ± 0.10

\*Lower limit.

<sup>†</sup>Subaru/FOCAS spectrum. <sup>‡</sup>Keck/LRIS spectrum.

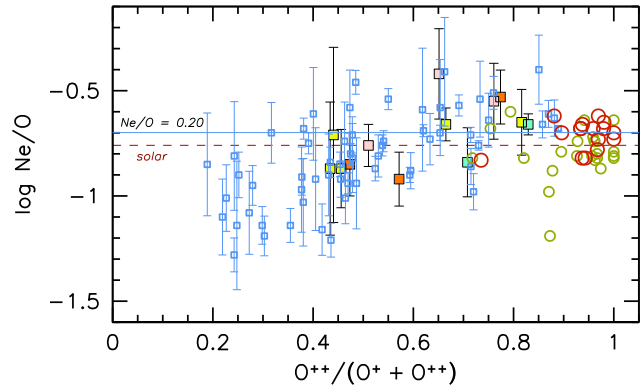
<sup>+</sup>Adopted abundances (weighted mean of Subaru and Keck results).

(Kwitter & Aller 1981; Vilchez et al. 1988; Crockett et al. 2006; Magrini et al. 2007; RS08). For consistency, we recomputed the PN and H II region abundances adopting the same techniques explained in Sect. 3.

Fig. 7 highlights the fact that the excitation of PNe is very high, with more than 75% of the oxygen in the O<sup>++</sup> ionization stage for most of the objects shown. The H II regions can be clearly separated from the majority of the PNe in Fig. 7a simply from their He<sup>++</sup>/H ratios, since He II λ4686, when observed in H II regions, never exceeds the intensity of a few percent of Hβ, while in planetary nebulae this line is often observed and can reach intensities similar to Hβ. The separation between PNe and H II regions is well displayed also by looking at N/O vs. O<sup>++</sup>/(O<sup>+</sup> + O<sup>++</sup>) in Fig. 7b. The average N/O ratio of the PNe is obviously larger than that for the H II regions, a result of the nucleosynthesis processes taking place in the advanced stages of evolution of the PNe stellar progenitors. This is also reflected by the large dispersion seen for the PN data, compared to the H II regions. Finally, in Fig. 7c we plot the ionic temperature T<sub>e</sub>[O III], derived from the [O III] λ4363/(λ4959 + λ5007) line ratio, as a function of the oxygen abundance. The general trend, for both PNe and H II regions, is of decreasing electron temperature with increasing metallicity. However, at any given O/H ratio, the PNe have higher T<sub>e</sub> values, as expected, and display a larger dispersion, which reflects the dispersion in stellar effective temperatures.

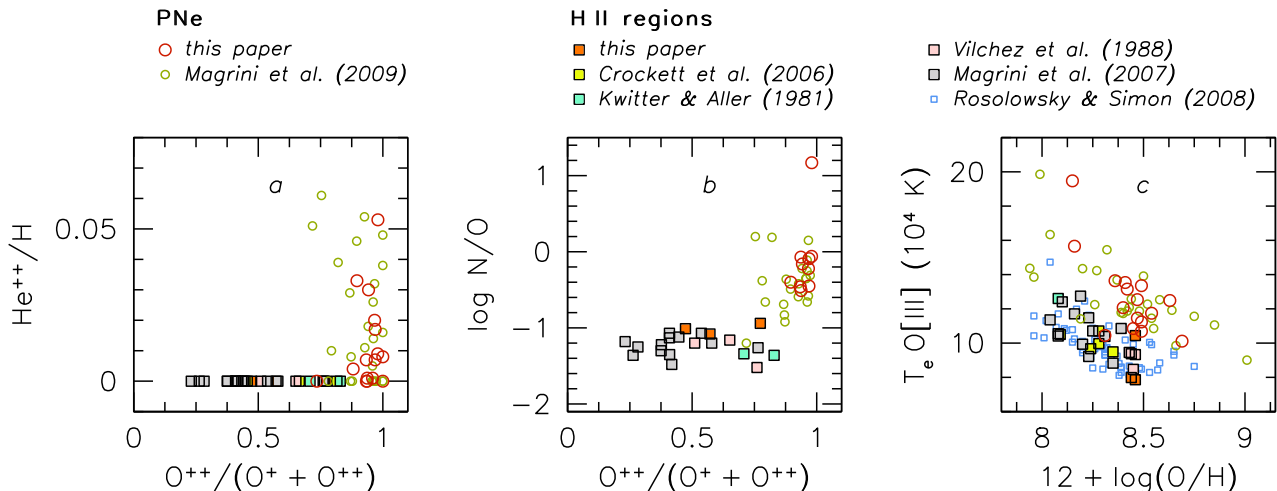
*Uncertainties in the ICFs?*

Fig. 8 shows how the H II region Ne/O ratio appears to decrease with excitation, in contrast with the expectation



**Figure 8.** The Ne/O ratio as a function of the excitation ratio O<sup>++</sup>/(O<sup>+</sup>+O<sup>++</sup>). Symbols as in Fig. 7. The error bars for the H II regions are shown. The horizontal dashed line represents the solar value log(Ne/O)<sub>⊙</sub> = -0.76 (Asplund et al. 2009). The mean Ne/O = 0.20 for the PNe in our sample is shown by the continuous blue line.

that this ratio should remain constant with variations of the nebular ionization structure. Since our neon abundances are derived from the single [Ne III] λ3868 line, this result can originate from an inaccurate correction for unseen ionization stages, in particular Ne<sup>+</sup>, when the O<sup>++</sup>/(O<sup>+</sup> + O<sup>++</sup>) ratio is below 0.5. However, it is unclear whether the discrepancy at O<sup>++</sup>/(O<sup>+</sup> + O<sup>++</sup>) < 0.5 is due to problems with the ICF(Ne) or to systematic errors in the data, because some of the low-excitation objects have a ‘normal’, approximately solar-like Ne/O ratio [log(Ne/O)<sub>⊙</sub> = -0.76 ± 0.11, Asplund et al. 2009, shown by the horizontal dashed line]. Moreover, some of the high-excitation H II regions signifi-



**Figure 7.** (a) He<sup>++</sup>/H abundance ratio as a function of the nebular excitation O<sup>++</sup>/(O<sup>+</sup> + O<sup>++</sup>). (b) N/O abundance ratio as a function of the nebular excitation. (c) electron temperature as a function of O/H. The objects plotted are: our new sample of PNe (red open circles), PNe in Magrini et al. (2009) with a [O III]  $\lambda$ 4363 detection (green open circles), H II regions with auroral line-based abundances from a compilation of data in the literature and the current work (squares). The sources for the data are summarized in the legend at the top.

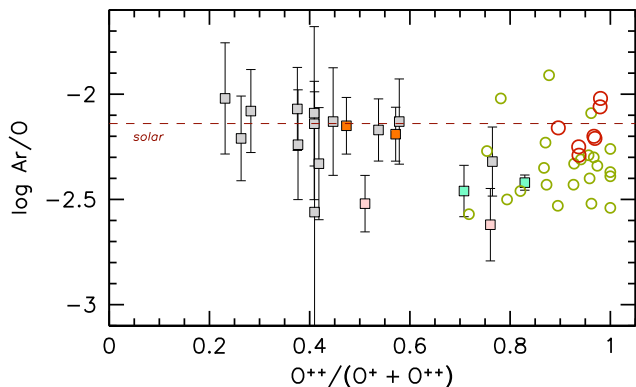


**Figure 9.** The Ar/O ratio as a function of the excitation ratio O<sup>++</sup>/(O<sup>+</sup> + O<sup>++</sup>). Symbols as in Fig. 7. The error bars for the H II region data points are shown. The horizontal dashed line represents the solar value log(Ar/O)<sub>⊙</sub> = -2.14 (Lodders 2003).

cantly exceed both the solar value and the PN values. We have considered alternative schemes for the ICF(Ne) of H II regions, such as those proposed by Izotov et al. (2006) and Pérez-Montero et al. (2007), but found even larger trends with excitation. We have therefore continued to adopt the ICF(Ne) from Kingsburgh & Barlow (1994) for the rest of this paper, in order to minimize the excitation dependence of the Ne/O ratio.

Considering only our PN sample, we obtain a mean  $\langle \text{Ne}/\text{O} \rangle = 0.20 \pm 0.03$ , shown by the continuous line in Fig. 8. We suggest to use this value as the representative Ne/O ratio in the ISM of M33, because the selected PNe are the objects with the highest excitation (and presumably with the most accurate abundances), and therefore the uncertainty in the total Ne abundance due to corrections for Ne<sup>+</sup> should be negligible.

As we explained earlier, for argon we have adopted the ICFs from Kingsburgh & Barlow (1994) for PNe and from Izotov et al. (2006) for H II regions. A plot of the Ar/O abun-

dance as a function of the excitation O<sup>++</sup>/(O<sup>+</sup> + O<sup>++</sup>) is shown in Fig. 9. As in the case of neon, the H II regions show a trend, this time with high-excitation objects having a lower Ar/O ratio than lower-excitation ones. The latter agree with the solar ratio, log(Ar/O)<sub>⊙</sub> = -2.14 ± 0.09 (Lodders 2003, indicated by the horizontal dashed line in Fig. 9). This suggests that the ICF(Ar) we are adopting is inadequate at O<sup>++</sup>/(O<sup>+</sup> + O<sup>++</sup>) > 0.6. We also point out the existence of a systematic offset of the Ar/O ratio between our PN sample (red circles), which agrees with the solar value, and the one based on the M09 data, which has a lower mean Ar/O. This could be related to observational errors, or could be due to the systematically higher extinction found by M09 (which would lower the [Ar III]  $\lambda$ 7135 strength relative to H $\beta$ ). For the following discussion we must therefore keep in mind that high-excitation H II regions and the M09 sample of PNe appear to have argon abundances that are under-estimated.

## 5 ABUNDANCE PATTERNS

### 5.1 Nitrogen and helium

The impact of the nucleosynthetic processes occurring in the PN progenitors on the chemical compositions of the ejected envelopes can be visualized in a plot of N/O vs. He/H (Fig. 10). Both N and He can be enhanced at the stellar surface during the red giant and AGB phases, largely depending on the mass and metallicity of the stellar precursors. The details are complicated by the combined effects of mechanisms such as mass loss, rotation, hot bottom burning and third dredge-up (Charbonnel 2005). The comparison between our new PN sample (mean log(N/O) = -0.27, excluding PN 78) and the H II region data (square symbols, with a mean log(N/O) = -1.22) shows a N/O enhancement on the order of one dex (the two mean values are shown as dashed lines in Fig. 10). When we factor in the radial trends (Sec. 6.2), the typical enhancement in N/O is  $\sim 0.8$  dex.

Stars belonging to the high end of the PN progenitor

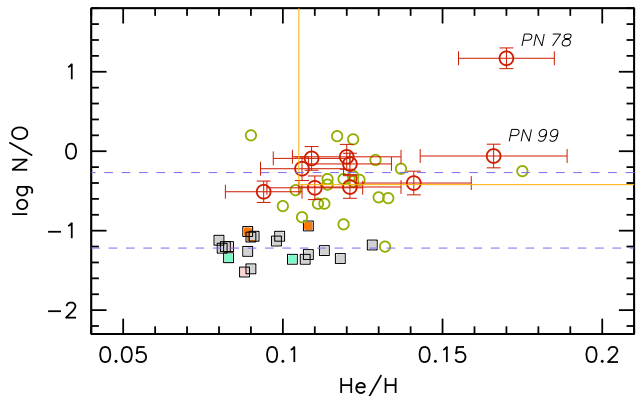


**Figure 10.** The N/O abundance ratio as a function of the He/H ratio. The boundaries defined by Torres-Peimbert & Peimbert (1997) for Type I PNe in the LMC ( $N/O > 0.38$ ,  $He/H > 0.105$ ) are drawn in orange. Symbols as in Fig. 7. Error bars are shown for our sample. The mean N/O ratio is drawn with dashed horizontal lines for the H II regions (lower line) and our PN sample (upper line).

mass spectrum (which extends approximately between 0.8 and  $8 M_{\odot}$ ) are associated with Type I PNe (Peimbert 1978), and are part of the youngest stellar population, showing clear N and He abundance excesses relative to the composition of H II regions, which represent the chemical makeup of the present-day ISM. The values of the minimum N/O and He/H ratios that define this class of PNe vary slightly between different authors, and need to account for the value of the N and O abundances in the ISM out of which the progenitor stars were formed (e.g. Stasińska, Richer, & McCall 1998; Leisy & Dennefeld 1996). Since the metal content of M33 is comparable to that of the LMC, we show in Fig. 10 the corresponding limits,  $N/O > 0.38$ ,  $He/H > 0.105$ , proposed by Torres-Peimbert & Peimbert (1997). With this definition, most of the PNe in our sample (red symbols with error bars) are of Type I, or have an N/O ratio that is compatible, given the errors, with being of Type I. However, it is worth pointing out that most of the PNe in our sample have N/O ratios that are only slightly above the Torres-Peimbert & Peimbert (1997) limit for inclusion into the Type I definition. In fact, we do not expect that a large number of PN progenitors in our sample, which is drawn from the brightest PNe in M33, experienced evolutionary phases that can strongly enhance the N/O ratio, such as hot bottom burning or second dredge-up, because the corresponding progenitor masses would be around  $2.5 M_{\odot}$ , according to the models of Marigo et al. (2004). Furthermore, the IMF would favor the detection of lower mass progenitors with respect to high mass ones.

### 5.1.1 The remarkable PN 78

The largest helium content in our PN sample ( $He/H \simeq 0.17$ ) is reached for PN 78 and PN 99 (both are identified in Fig. 10). The former also has a striking nitrogen excess,  $12 + \log(N/H) = 9.20$  and  $\log(N/O) = 1.09$ . The large N content does not depend on the correction factor scheme that we used, and is due to the strong nitrogen lines observed (the strength of  $[N II] \lambda 6583$  is approximately twice that of

$H\alpha$ ; see the spectrum in Fig. 2). The high electron temperature is accompanied by a very high nebular excitation, with the only detection of  $[Ar V] \lambda\lambda 6435, 7005$  in our sample.

The nitrogen enrichment that we derive for PN 78 is comparable to the maximum observed to date in Type I PNe belonging to the Milky Way (e.g. Stanghellini et al. 2006), although it occurs at a much lower O/H ratio. In fact, PN 78 has the lowest measured oxygen abundance in our sample,  $12 + \log(O/H) = 8.15$ , considerably lower than the median of 8.47. It is tempting to interpret these data as the result of hot bottom burning in a massive progenitor ( $\sim 5 M_{\odot}$ ), which could explain both the low O and the high N abundances, with nitrogen synthesized at the expense of C. At sufficiently high temperatures N could be produced at the expense of oxygen in the ON cycle. However, in the case of PN 78 the latter possibility seems to be excluded. We plot in Fig. 11 the N/O ratio as a function of N/H. The regression line to the whole PN sample (excluding PN 78), calculated accounting for errors in both coordinates (we used an IDL adaptation of the routine *fitexy* by Press et al. 1992 for this and subsequent fits of this kind), has a slope of  $0.99 \pm 0.01$ , indicating that the N/O enhancement relative to H II regions is due primarily to high N production, rather than O depletion. This appears to hold for the M33 PN sample as a whole, and also for the specific case of PN 78. In addition, both the Ar/O and Ne/O ratios for PN 78 are comparable to those of the rest of the sample, confirming that oxygen is not significantly depleted.

PNe observed in the Milky Way and the Magellanic Clouds have generally much smaller N/H ratios than we find in PN 78, which is interpreted as a modest efficiency of hot bottom burning in intermediate-mass precursors (Marigo et al. 2003), since a larger efficiency would lead to an overproduction of N. Our data for PN 78 seem to suggest that, occasionally, large N/H and N/O ratios can be encountered, simultaneously with a large He/H ratio (the latter as a result of an efficient third dredge-up).

Richer & McCall (2007) have presented chemical abundances for PNe in the irregular galaxy NGC 6822. One of their targets, S33, with  $12 + \log(N/H) = 8.93$  and  $\log(N/O) = 0.90$ , has a nitrogen excess similar to PN 78 in M33. In this case, however, the oxygen abundance,  $12 + \log(O/H) = 8.03$ , is *larger* than the galaxy's mean value. These authors propose that this could be an example of a star in which oxygen has been dredged-up in the late evolutionary phases. The high N/O ratio is not explicitly discussed by Richer & McCall (2007), although they note that, in general, nitrogen should be more easily dredged-up than oxygen.

## 5.2 Neon and oxygen

Since core-collapse supernovae (massive stars with initial  $M > 8 M_{\odot}$ ) are the main sites of oxygen and neon production, one expects that, unless important nucleosynthesis of these elements takes place in the less massive stars that are the PN precursors, their variation occurs in lockstep in PNe, similarly to the case of H II regions. This is in fact observed in the Milky Way and the Magellanic Clouds (Henry 1989; Leisy & Dennefeld 2006), and is normally taken as evidence that the oxygen abundance measured in PNe is equivalent to that of the progenitor stars at the moment of birth (Richer & McCall 2007). Deviations from this re-

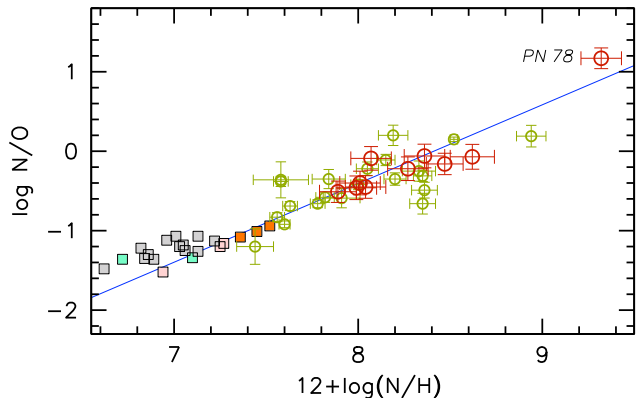


**Figure 11.** The N/O abundance ratio as a function of the N/H ratio. Symbols as in Fig. 7. The regression to the PN data is represented by the continuous line.

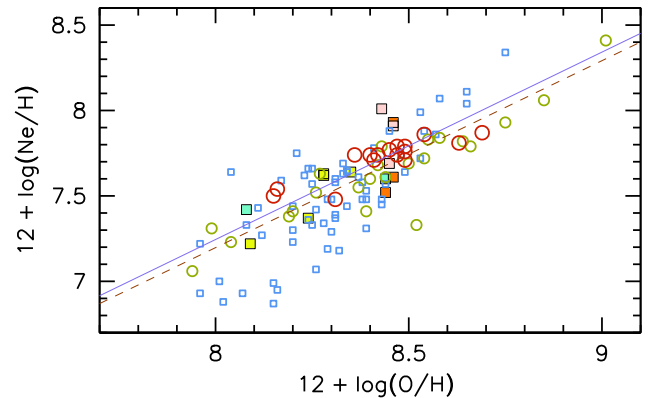
sult have been discovered in low metallicity environments, where third dredge-up episodes could be more efficient, with the consequence that oxygen can be overabundant in PNe relative to H II regions, as both theory (Marigo 2001) and observations (Magrini et al. 2005; Peña, Stasińska, & Richer 2007; Kniazev, Pustilnik, & Zucker 2008) suggest. However, according to Richer & McCall (2007) these findings constitute the exception rather than the rule, perhaps because most progenitors of the bright PNe studied spectroscopically in other galaxies are of rather small mass ( $< 1.5 M_{\odot}$ , Richer & McCall 2008).

Fig. 12 shows the values of Ne/H as a function of O/H for PNe and H II regions, with the same symbols as in Fig. 7. The regression to the PN data (considering [O III]  $\lambda 4363$ -based abundances only), shown by the dashed line, has a slope of  $1.09 \pm 0.07$ , with a correlation coefficient of 0.89. The Ne-O relationship observed by Izotov et al. (2006) in a sample of star-forming galaxies and blue compact galaxies is shown for reference (continuous line, slope  $1.097 \pm 0.015$ ). The increasing deviation of the RS08 H II region data (blue squares) from the Izotov et al. line with decreasing O/H has the same nature as the excitation trend we detected in the Ne/O ratio (Fig. 8), and can be related to an inaccurate ICF(Ne) at low nebular excitation.

Wang & Liu (2008) have pointed out that the Ne/O ratio of the ionized ISM follows an increasing trend with O/H, reaching a mean value of  $\sim 0.25$  in the Milky Way and other metal-rich galaxies, suggesting that the Ne enrichment of the ISM is delayed relative to O. The average Ne/O ratio for PNe with [O III]  $\lambda 4363$  detections in M33 (our sample + M09) is  $0.18 \pm 0.04$ , comparable with the value observed in the LMC (Leisy & Deneffeld 2006), which has a present-day metallicity similar to that of the ISM in M33.

### 5.3 Argon and oxygen

Argon and sulfur are also products of primary nucleosynthesis in massive stars, and their abundances can be used in alternative to oxygen to characterize the initial composition of PN progenitors, since they should not be affected by evolution during the AGB phase (Leisy & Deneffeld 2006), at any chemical composition. The main difficulty in the study of argon and sulfur is that observationally it is more chal-



**Figure 12.** Ne/H as a function of O/H. Symbols as in Fig. 7. The regression to the PNe (our sample + M09) is shown by the dashed line, and the trend found by Izotov et al. (2006) for more than 400 emission-line galaxies is shown by the continuous line.

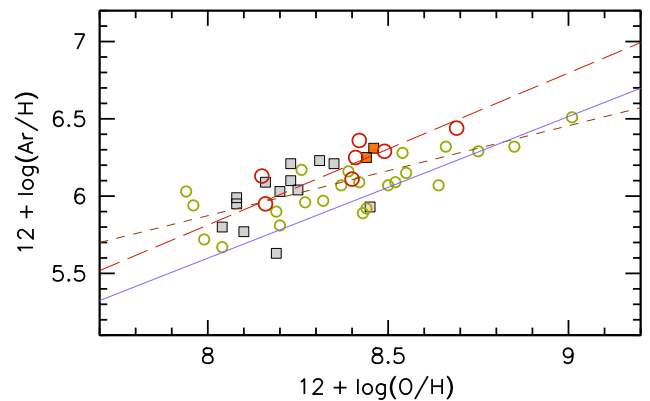


**Figure 13.** The Ar/H abundance ratio as a function of O/H. Symbols as in Fig. 7. The regression to the PNe (our sample + M09) is shown by the short-dashed line, and the trend found by Izotov et al. (2006) for more than 400 emission-line galaxies is shown by the continuous line. The long-dashed line represents the regression to our PN sample, combined with the H II regions.

lenging than that of oxygen, due either to the weakness of the lines, or the required wavelength coverage. Moreover, the correction for unseen stages of ionization can be important, especially for sulfur (Henry et al. 2004). In this work we only consider the abundance of argon, since for sulfur we only have access to the [S II] lines.

Observations in the Milky Way have shown that argon, like neon, follows oxygen reasonably well in both PNe and H II regions (Henry et al. 2004), although Stanghellini et al. (2006) failed to find a correlation between Ar and O abundances for PNe, likely as a result of the uncertain Ar abundances. Our plot of Ar/H vs. O/H is shown in Fig. 13, where we can see a good correlation ( $R_{xy} = 0.76$ ) between the two quantities. The slope of the regression that considers the whole PN sample (short-dashed line) is  $0.58 \pm 0.09$ , significantly lower than unity, and smaller than the value found for the star-forming galaxy sample studied by Izotov et al. (2006),  $0.916 \pm 0.021$ . For Milky Way PNe, Henry et al. (2004) obtained a good correlation between Ar/H and O/H, but with an even higher slope of  $1.34 \pm 0.14$ . In light of the

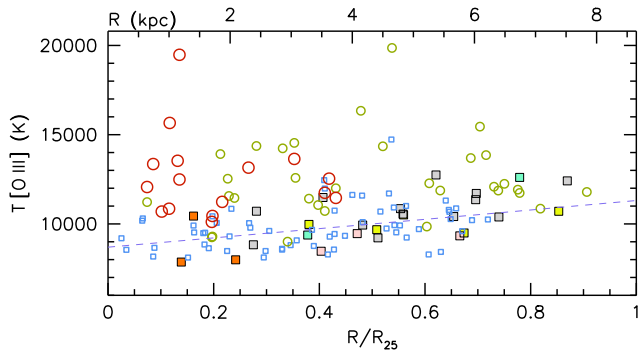


**Figure 14.** Nebular temperature  $T[\text{O III}]$  as a function of galactocentric distance for PNe and H II regions. Radial distances are given both in terms of the isophotal radius  $R_{25}$  (bottom axis) and in kpc (top axis). Symbols as in Fig. 7. The dashed line represents the linear regression to the H II region data.

problems with the PN Ar/H abundances mentioned earlier, we carried out a regression to our PNe sample and the H II regions combined, since they appear to follow a common relation in the diagram (long-dashed line). We find a slope of  $0.98 \pm 0.27$ , consistent with unity, although the error is quite large. We point out that these data lie systematically above the Izotov et al. (2006) regression line. We conclude that Ar is rather well correlated with O in both PNe and H II regions in M33, but further studies will be required to reduce the uncertainty in the relation between these two quantities for this galaxy.

## 6 RADIAL ABUNDANCE GRADIENTS

One of our main motivations at the inception of this spectroscopic study of M33 was to test whether PNe could provide complementary information on the galactic-scale oxygen abundance gradient in this galaxy and on its possible temporal evolution. Despite the fact that several H II region emission line studies have been carried out in M33 throughout the years (to cite a few: Kwitter & Aller 1981; Vílchez et al. 1988; Willner & Nelson-Patel 2002; Crockett et al. 2006; Magrini et al. 2007; Rosolowsky & Simon 2008; Rubin et al. 2008), the present day metal content of the central parts of the galaxy remains the most uncertain, due to the difficulties in measuring the required, temperature-sensitive faint auroral lines, as the gas temperature decreases with decreasing galactocentric distance. This is a consequence of the nebular cooling increasing with metallicity. Fig. 14 illustrates the systematic change of temperature with distance from the galactic center derived for the H II regions, for which we find a gradient of  $300 \pm 60 \text{ K kpc}^{-1}$  (no galactocentric variation in temperature is detected for PNe).

Comparative studies of the abundance gradient in the Milky Way, that include observations of PNe, H II regions and young stars, provide rather consistent results among the different abundance tracers (Maciel & Quireza 1999; Henry et al. 2004), but with considerable uncertainties resulting from poorly known distances to individual targets. Chemical elements that are unaffected by nucleosynthesis in low- and intermediate-mass stars, such as S, Ar and Cl, should preferentially be used, however it appears that O and

Ne, which are more easily measured, also trace the abundances of the ISM at the time of formation of the PNe progenitors, since their production is very small in the corresponding mass range, except at the lowest metallicities.

Our discussion about the Ne/O ratio presented in Section 5.2 confirms the general finding obtained by other authors in a few nearby galaxies, namely that above the metallicity of the SMC [ $12 + \log(\text{O}/\text{H}) = 8.1$ ] the brightest PNe and H II regions have comparable metallicities, as measured by the O/H ratio (Richer 1993; Richer & McCall 2007). This allows us to examine the metallicity gradient in M33 independently of the H II regions, by using PNe. In the comparison, we can also include massive supergiant stars, which, owing to their young ages, are also excellent probes of the present day chemical composition of galaxies. In a recent work on the spiral galaxy NGC 300, Bresolin et al. (2009) confirmed that the analysis of the metal lines of blue supergiants provides an abundance gradient which is in excellent agreement with the one derived from [O III]  $\lambda 4363$  detections in H II regions, including metallicities near the solar value. In the case of M33, stellar metallicities for young stars have been published by Urbaneja et al. (2005, B supergiants) and U et al. (2009, A supergiants). The latter also compared the radial abundance gradient in M33 using different indicators (H II regions, supergiant stars and Cepheids).

Despite the difficulties of obtaining spectra of extragalactic PNe with good signal-to-noise ratios, the use of PNe presents a couple of advantages over H II regions in abundance studies near the galactic central regions. First, as the metallicity increases at small galactocentric distances, the determination of the decreasing H II region electron temperature becomes very difficult, as a consequence of the more efficient gas cooling that reduces the strengths of the [O III] lines. In the case of PNe, the excitation provided by the much harder stellar radiation and the higher electron densities, which reduce the cooling due to collisional de-excitation, ensure that the detection of [O III]  $\lambda 4363$  is still feasible. Secondly, PNe are not expected to be affected by abundance biases at high O/H ratios. Stasińska (2005) pointed out that in the presence of temperature gradients *within* H II regions, which are predicted to develop at high metallicity (around and above the solar value), the measured O/H abundances could systematically underestimate the true metal content of the gas. Again, the high effective temperature of the ionizing stars of PNe, together with their higher densities, prevents this from occurring.

In the following discussion, we consider optical comparison samples of H II regions taken from various authors: Kwitter & Aller (1981), Vílchez et al. (1988), Crockett et al. (2006), Magrini et al. (2007) and RS08. These works provide [O III]  $\lambda 4363$  detections for the measurement of the electron temperature. The wavelength coverage differs among the different studies, so that, for example, [N II] and [Ar III] fluxes are unavailable for the Crockett et al. (2006) and RS08 samples. Only nebulae for which the electron temperature could be directly derived from [O III]  $\lambda 4363$  were retained, leaving a final sample of 88 nebulae. To overcome difficulties in the analysis arising from the non-homogeneous nature of the data sets and to avoid systematic discrepancies that could originate from differences in atomic data, ionization correction factors, etc., we have recalculated

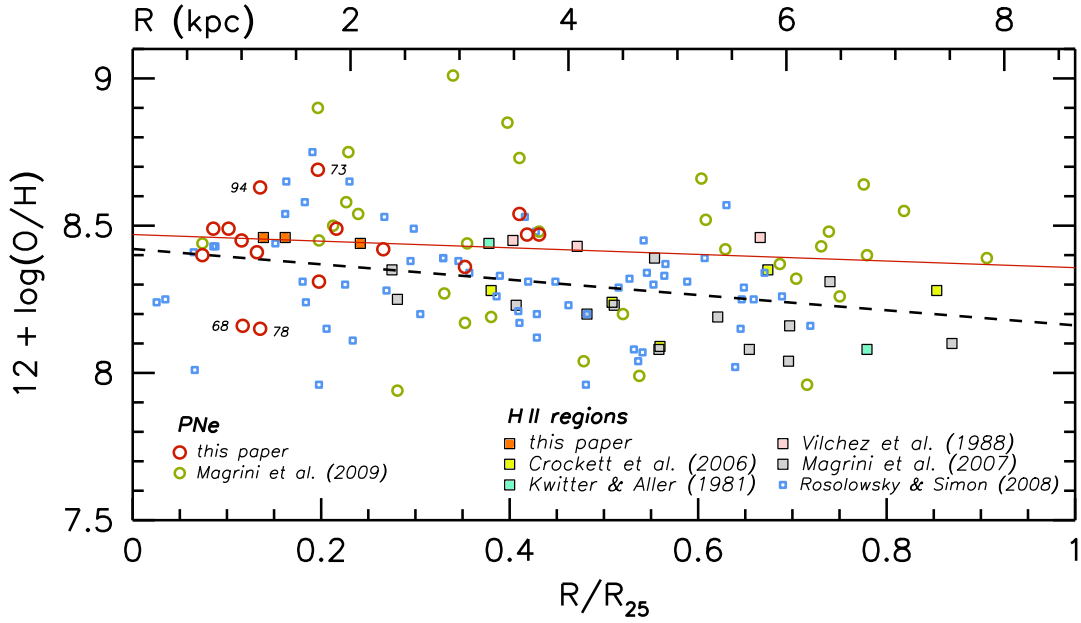


**Figure 15.** O/H radial gradient for PNe and H II regions. Radial distances are given both in terms of the isophotal radius  $R_{25}$  (bottom axis) and in kpc (top axis). The different symbols used are summarized in the legend. Linear regressions are shown by the red continuous line (PNe) and the dashed black line (H II regions). The four planetaries that deviate the most from the PNe regression, PN 68, 73, 78 and 94, are labeled.

the abundances from the published line fluxes using the same procedure employed for our H II region data (see Section 3).

### 6.1 Oxygen

The O/H radial behaviour for the PNe having [O III]  $\lambda 4363$ -based abundances is compared with the H II region and the blue supergiant gradients in Fig. 15 and 16, respectively. We have calculated a linear regression for the combined PNe data (ours and M09), and represent it with the continuous red lines in both figures. We have used the weighted least square method described by Akritas & Bershadsky (1996), to account for the intrinsic scatter in abundance, in addition to uncertainties in the individual abundance values. The regression yields:

$$12 + \log(\text{O}/\text{H}) = 8.47 (\pm 0.07) - 0.013 (\pm 0.016) R_{\text{kpc}} \quad (1)$$

The gradient slope that we obtain is compatible within  $1-\sigma$  with both a flat gradient and with the slope obtained by M09 ( $-0.031 \pm 0.013 \text{ dex kpc}^{-1}$ ). We note that M09 did not restrict their analysis to objects with auroral line detections, as we do instead. This partly explains the difference in the regression parameters between the two studies. Moreover, our measurements of [O III]  $\lambda 4363$  in the central 2 kpc of the galaxy provide additional constraints for the gradient slope in the inner disk.

The linear regression to the H II region sample, shown by the dashed line in Fig. 15, is:

$$12 + \log(\text{O}/\text{H}) = 8.42 (\pm 0.03) - 0.030 (\pm 0.008) R_{\text{kpc}} \quad (2)$$

Again, this is compatible with the slope of the PNe O/H abundance gradient. Where the PN and H II region samples differ is in the intrinsic scatter, which is 0.20 dex and 0.09 dex, respectively (and easily confirmed qualitatively by

inspecting Fig. 15). However, it is possible that the measurement errors for the M09 data have been under-estimated, because restricting the regression to our new PN sample the scatter is considerably smaller,  $0.09 \text{ dex}$  (with slope  $-0.027 \pm 0.032 \text{ dex kpc}^{-1}$ ), confirming the suggestion made earlier that the abundances measured by M09 are less precise than those we measure in our new sample. One can, in principle, expect a larger scatter for PNe than for H II regions, due to the fact that PNe sample a significant age range in the evolution of galaxies. We point out that even in our new sample two PNe (PN 73 and PN 94) located in the inner 2 kpc have an approximately solar oxygen abundance ( $12 + \log(\text{O}/\text{H})_{\odot} = 8.69$ , Asplund et al. 2009), deviating considerably ( $+0.2 \text{ dex}$ ) from the regression line that describes the abundance gradient. At the same time, PN 68 and PN 78 lie  $\sim 0.3 \text{ dex}$  below the regression.

We conclude that, given the uncertainties, bright PNe and H II regions give a similar picture of the oxygen abundance gradient in M33. Our PNe sample provides a good number of auroral line-based abundances in the central region of M33, where H II region abundances are more difficult to obtain, due to the nebular cooling. The ionized gas does not suggest deviations from a simple exponential gradient in O/H vs. radius, even in the central region of the galaxy.

The linear regression to the B-type supergiants studied by Urbaneja et al. (2005), shown in Fig. 16 by the dashed line, is given by:

$$12 + \log(\text{O}/\text{H}) = 8.61 (\pm 0.11) - 0.041 (\pm 0.027) R_{\text{kpc}} \quad (3)$$

The O/H gradient slope from the blue supergiants is slightly steeper than that obtained from the ionized gas, although considering the errors the stellar gradient is still compatible with the gradient obtained from PNe and H II regions (it is worth noting that the single star at  $R = 7.22 \text{ kpc}$  is largely responsible for the steeper slope). In conclu-

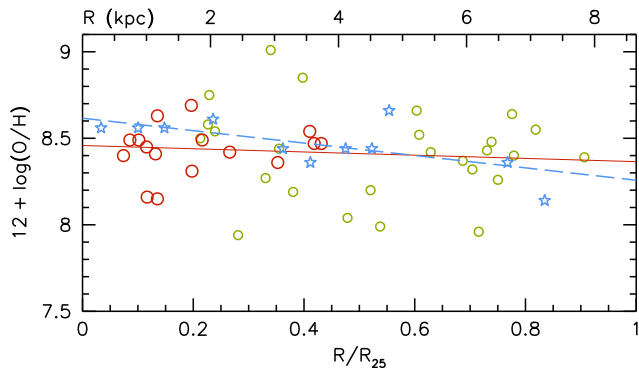


**Figure 16.** O/H radial gradient for PNe (red and green circles) and B-type supergiants (blue star symbols). Linear regressions are shown by the red continuous line and the dashed blue line, respectively.

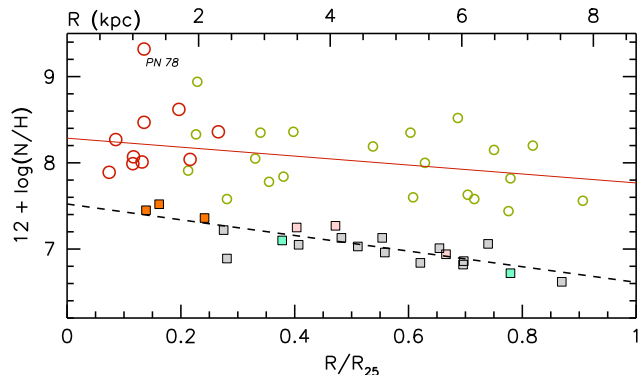


**Figure 17.** N/H radial gradient for PNe and H II regions. Symbols and lines as in Fig. 15. PN 78 was excluded from the PN linear regression.

sion, the oxygen abundance indicators at our disposal (PNe, H II regions and B supergiants) provide a consistent picture of the O/H gradient in M33.

## 6.2 Nitrogen

The radial N/H abundance gradient for both H II regions and PNe is shown in Fig. 17. The H II regions display a well-defined gradient, with a slope  $-0.105 \pm 0.015$  dex  $\text{kpc}^{-1}$ , i.e. significantly steeper than for O/H. The slope for the PNe is somewhat shallower ( $-0.060 \pm 0.027$  dex  $\text{kpc}^{-1}$ ), but with a much larger scatter (0.31 dex vs. 0.09 dex; we excluded the high N/H abundance PN 78 from the fit). If we interpret the H II region N/H ratios as the original abundances of the PNe progenitors at birth, the clear offset we see between H II regions and PNe in Fig. 17 is a signature of the nitrogen enrichment that took place during the AGB phase of the PN progenitors.

The effect of nitrogen enrichment on the N/O radial abundance gradient is displayed in Fig. 18, where we point out that the two regressions for the H II regions and the PNe are virtually parallel (the slopes are  $-0.052 \pm 0.015$  and  $-0.044 \pm 0.025$  dex  $\text{kpc}^{-1}$ , respectively). The nitrogen enrichment in the PN progenitors is approximately constant, about 0.8 dex, across the metallicity range covered by our samples. A similar result was found by Richer & McCall

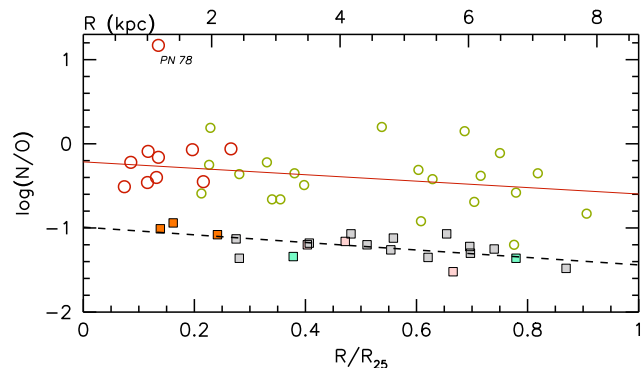


**Figure 18.** N/O radial gradient for PNe and H II regions. Symbols and lines as in Fig. 15. PN 78 was excluded from the PN linear regression.

(2007) in the case of the SMC (where the offset between H II regions and PNe was found to be  $\sim 0.7$  dex), but in other dwarf irregulars these authors observed that the N/O ratios span a very wide range ( $\sim 2$  dex) for a given O/H ratio, so it does not seem possible to generalize our result, even though the N/O range in M33 appears relatively smaller. We also note that a few PNe have N/O ratios comparable to those of the H II regions, thus their progenitors did not produce large quantities of nitrogen, perhaps as a consequence of their lower masses. Although admittedly the statistics are rather poor, the data in Fig. 19, where we plot N/O vs. O/H, suggest that this is happening preferentially at higher metallicity [ $12 + \log(\text{O}/\text{H}) > 8.5$ , although this might depend on a poor abundance determination], and that the N/O ratio, and therefore the nitrogen enrichment, is larger at smaller O/H (a similar result was found, among others, by Leisy & Dennefeld 1996 and Stasińska et al. 1998; but note that, given the errors, the regressions in Fig. 19 are consistent with flat slopes).

In Fig. 19 we also include the N/O ratios calculated for B-type supergiants by Urbaneja et al. (2005, blue star symbols). In these post-main sequence stars rotationally-induced mixing of material processed in the stellar core can be brought up to the photosphere (Maeder & Meynet 2000). The N/O abundance ratio, in particular, is heavily enhanced in B supergiants, likely by internal mixing, although additional mechanisms (such as binarity and magnetic fields) can also play an important role (Hunter et al. 2008). B supergiants with even larger N/O ratios could be explained by the deep convection occurring during the red supergiant phase, although current theoretical tracks do not extend back to the blue (Hunter et al. 2009). The stellar data points in Fig. 19, compared to the H II regions, show that, interestingly, the N/O ratio in the B supergiants is approximately the same as for the majority of the PNe, indicating that the nitrogen enrichment of present-day evolved massive stars ( $20\text{--}40 M_{\odot}$ ) is comparable to that of the progenitor stars of bright PNe ( $\sim 2 M_{\odot}$ ).

## 6.3 Neon and argon

The top portion of Fig. 20 displays the radial Ne/H abundance gradient, where we have excluded H II regions with  $\text{O}^{++}/(\text{O}^{++} + \text{O}^{+}) < 0.5$ , since we have evidence that

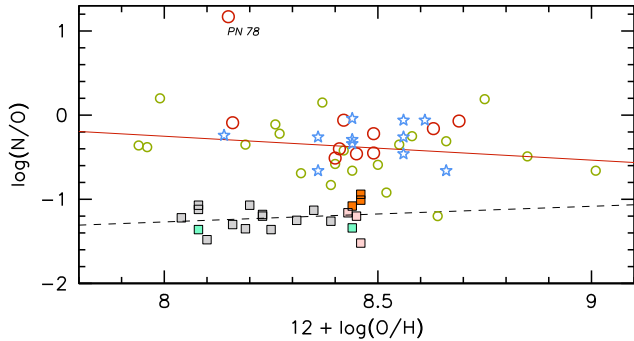


**Figure 19.** N/O for PNe, H II regions and B-type supergiants as a function of O/H. Symbols and lines as in Fig. 15 and 16. PN 78 was excluded from the PN linear regression.

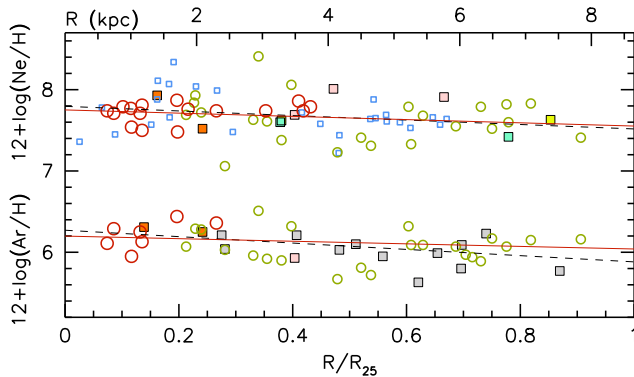


**Figure 20.** Ne/H (top) and Ar/H (bottom) radial gradients for PNe and H II regions. Symbols and lines as in Fig. 15.

the ICF may be wrong for those. The slopes we obtain for H II regions and PNe,  $-0.032 \pm 0.020$  and  $-0.023 \pm 0.018$  dex kpc $^{-1}$ , respectively, are consistent with each other and with the O/H gradient slope. We must add that for the H II regions the value of the slope is sensitive to the adopted selection in the excitation parameter: if we remove from the fit the H II regions for which  $O^{++}/(O^{++} + O^+) < 0.6$ , for example, we obtain a slope of  $-0.054 \pm 0.018$  dex kpc $^{-1}$ , more in agreement with the result obtained from Spitzer observations by Rubin et al. (2008),  $-0.058 \pm 0.014$  dex kpc $^{-1}$ .

In the bottom plot of Fig. 20 we show the radial gradient of the Ar/H abundance ratio for PNe and H II regions. We have omitted the 4 H II regions with  $O^{++}/(O^{++} + O^+) > 0.6$ . The gradient slope we show for the PNe is affected by the additional uncertainty represented by the systematic offset we noticed between our sample and the one by M09. This uncertainty is not reflected in the gradient parameter summary of Table 8. As the table shows, the slopes we derive for both types of objects agree with the values obtained for the oxygen abundance gradient.

#### 6.4 Radial gradient summary

To summarize our results for this section, we report in Table 8 the parameters of the radial logarithmic abundance gradients for O, N, Ar and Ne. The number of objects used for the fits is included. Given the sources upon which these

results are based, it is not surprising that we find a good agreement with the slopes obtained for PNe by M09 (O/H:  $-0.031 \pm 0.013$  dex kpc $^{-1}$ ; Ne/H:  $-0.037 \pm 0.018$  dex kpc $^{-1}$ ).

It can be seen from Table 8 that, considering PNe and H II regions separately, the slopes for the O, Ar and Ne abundance gradients are consistent with each other. In an attempt to reduce the errors for a representative  $\alpha$ -element gradient slope, we have combined the abundance data for O, Ar and Ne, separately for PNe and H II regions, adjusting the zero-points by the intercept amounts reported in Table 8. A regression to the combined data yields

$$\frac{d \log(\alpha/H)}{dR} = -0.033 \pm 0.008 \text{ dex kpc}^{-1}$$

for H II regions, and

$$\frac{d \log(\alpha/H)}{dR} = -0.018 \pm 0.010 \text{ dex kpc}^{-1}$$

for PNe. The two slopes agree within the 1- $\sigma$  errors. If there has been an evolution of the gradient with time, it remains undetected with our current uncertainties. Combining the results, we obtain a representative slope of the radial gradient of the  $\alpha$ -elements in the ISM of M33:

$$\text{ISM} : \frac{d \log(\alpha/H)}{dR} = -0.025 \pm 0.006 \text{ dex kpc}^{-1}$$

We also point out that the M33 central abundances of these  $\alpha$ -elements are in good agreement between PNe and H II regions. For oxygen we find a weighted central abundance  $12 + \log(O/H)_c = 8.43 \pm 0.02$ . With the adopted solar ratio [ $12 + \log(O/H)_\odot = 8.69$ , Asplund et al. 2009], this corresponds to  $0.55 \pm 0.03$  times the solar value. Argon yields a similar result,  $0.50 \pm 0.08$  solar, while the neon central abundance equals  $0.69 \pm 0.04$  times the solar value (note that we prefer to adopt the Lodders 2003 solar value for Ar/H, which is 0.15 dex larger than the Asplund et al. 2009 value). The slightly discrepant result for Ne could be brought to a better agreement with those for O and Ar if we adopted a higher solar value for Ne/O, as advocated in a few recent studies (e.g. Wang & Liu 2008). A solar value  $(\text{Ne/O})_\odot = 0.22$  would bring agreement between the central O and Ne abundances in M33, relative to solar (the most recent Asplund et al. 2009 value is  $(\text{Ne/O})_\odot = 0.17$ ).

## 7 CONCLUSION

Our work highlights the importance of deriving auroral line-based chemical abundances for large samples of planetary nebulae and H II regions in nearby galaxies. These observations are essential to learn more about systematic errors in nebular diagnostics, the time evolution of the chemical composition of star-forming galaxies, and the nucleosynthesis of intermediate-mass stars. Key targets for these studies are nearby irregular and spiral galaxies, where the spectroscopy of faint diagnostic lines can be carried out with the present generation of telescopes and instruments.

We have obtained new deep optical spectrophotometry of 16 planetary nebulae in M33, mostly located in the central two kpc of the galaxy. For this sample we have derived

Table 8. Parameters of linear radial abundance gradients<sup>1</sup>.

Element	PNe				H II regions			
	Slope (dex kpc <sup>-1</sup> )	Intercept	Correlation Coefficient	No. objects	Slope (dex kpc <sup>-1</sup> )	Intercept	Correlation Coefficient	No. objects
O.....	-0.013 ± 0.016	8.47 ± 0.07	-0.10	48	-0.030 ± 0.008	8.42 ± 0.03	-0.34	87
N.....	-0.060 ± 0.027	8.29 ± 0.12	-0.38	36	-0.105 ± 0.015	7.52 ± 0.07	-0.83	21
Ar.....	-0.018 ± 0.014	6.20 ± 0.06	-0.27	36	-0.045 ± 0.016	6.27 ± 0.07	-0.60	15
Ne.....	-0.023 ± 0.018	7.75 ± 0.07	-0.17	45	-0.032 ± 0.020	7.79 ± 0.08	-0.27	35

<sup>1</sup>Linear relation between  $12 + \log(X/H)$  and galactocentric distance in kpc.

electron temperatures and chemical abundances from the detection of the [O III]  $\lambda 4363$  line. After combining our abundances with those we obtained with the same direct method from the emission line observations of Magrini et al. (2009, 32 PNe), we have examined the behavior of nitrogen, neon, oxygen and argon in relation to each other in PNe and H II regions, and as a function of galactocentric distances.

The N/O and He/H abundance ratios of most of the PNe of our new sample, which comprises objects in the brightest 1.5 magnitudes of the [O III]  $\lambda 5007$  luminosity distribution, lead to a Type I classification, which, at least in the Milky Way, corresponds to young objects with relatively massive progenitors. We have found one object, PN 78, with an extreme nitrogen abundance, accompanied by a large helium content.

We confirm the good correlation between Ne/H and O/H abundances for PNe in M33, as expected from the primary nature of these two elements. We also find a linear correlation between argon and oxygen, but we point out that this is somewhat uncertain, due possibly to observational errors. The Ar/O ratio is consistent with the value found in H II regions and in the Sun. For Ne/O, we find a mean value for PNe of 0.20, which is 18% larger than the Asplund et al. (2009) value, but in agreement with the Ne/O vs. O/H trend found by Wang & Liu (2008). These result lend support to the idea that at the metallicities of the PNe analyzed in M33 these three  $\alpha$ -elements (O, Ar and Ne) trace the abundance of the progenitor stars at the moment of their birth, and in particular that neon and oxygen have not been modified during the dredge-up process taking place during the AGB phase.

We find no significant abundance offset between PNe and H II regions at any galactocentric radius, despite the fact that they represent different age groups in the evolution of the galaxy. The combination of the PN and H II region auroral-line abundances provide information on the shape of the oxygen abundance gradient in the central few kpc of M33. We obtain an  $\alpha$ -element abundance gradient of the ISM in M33 with a slope of  $-0.025 \pm 0.006$  dex kpc<sup>-1</sup>, and the slopes obtained separately for H II regions and PNe agree, within the current uncertainties. This is consistent with the conclusion by M09 that the disk of M33 has not experienced a significant chemical enrichment of its interstellar medium in the past few Gyr. Moreover, despite the large dispersion in O/H abundances for both PNe and H II regions, we find no indication that towards the center of the galaxy PN values are systematically larger than H II region

ones, as would be the case if H II region abundances were biased towards lower values, and as could be the case if O/H in the central parts of M33 were really high (super-solar). This confirms what B supergiants already indicated for this galaxy.

The growing amount of data on abundance tracers in M33 in the past few years has raised new questions regarding the present-day abundance gradient in this galaxy. For example, what is the origin of the large intrinsic dispersion of H II region O/H abundances (also displayed by the PNe data shown here) at a given radius discovered by RS08? We found no correlation of the abundance residuals, as measured with respect to the mean gradient, with a number of parameters, including nebular luminosity, equivalent width of the H $\beta$  line, line strengths, gas density, or position in the galaxy disk. An analysis of additional data acquired as part of the M33 Metallicity Project (RS08) will hopefully shed some light on this issue. Moreover, the study of A supergiants by U et al. (2009) provided metallicities near the galaxy center that lie above the solar value, and their derived slope, corrected to account for our adopted distance, is  $-0.084 \pm 0.010$  dex kpc<sup>-1</sup>. While it is true that the comparison between stars and ionized gas is complicated by the fact that A supergiant metallicities refer mostly to the iron content (rather than that of the  $\alpha$ -elements), it is striking, as also pointed out by U et al. (2009), that the stellar metallicities are consistently near or above the solar value close to the center of M33, while the H II regions samples includes objects with O/H ratios that extend down to 20% of the solar value. Future studies of the oxygen content of A and B supergiants in the central few kpc of M33 will help to directly compare stellar and nebular abundances, and perhaps better understand the nature of the abundance dispersion.

FB would like to thank the Observatoire de Paris (Meudon) and the Instituto de Astrofísica de Andalucía (Granada) for hospitality during visits in which part of this work was carried out. FB gratefully acknowledges the support from the National Science Foundation grant AST-0707911. ER's work is supported by a Discovery Grant from NSERC of Canada. We thank L. Magrini, for providing us with data in advance of publication, and the staff of the Subaru telescope, in particular T. Hattori, for the support provided for this project. We are grateful to the referee, Jeremy Walsh, for providing comments that helped us to improve the manuscript.

## REFERENCES

- Aggarwal, K. M., & Keenan, F. P. 1999, *ApJS*, 123, 311
- Akritas, M. G., & Bershad, M. A. 1996, *ApJ*, 470, 706
- Asplund, M., Grevesse, N., Sauval, A. J., & Scott, P. 2009, *ARAA*, 47, 481
- Bonanos, A. Z., Stanek, K. Z., Kudritzki, R. P., et al. 2006, *ApJ*, 652, 313
- Boulesteix, J., Courtes, G., Laval, A., Monnet, G., & Petit, H. 1974, *A&A*, 37, 33
- Bresolin, F., Gieren, W., Kudritzki, R., Pietrzyński, G., Urbaneja, M. A., & Carraro, G. 2009, *ApJ*, 700, 309
- Charbonnel, C. 2005, in *AIP Conf. Ser.*, Vol. 804, *Planetary Nebulae as Astronomical Tools*, ed. R. Szczerba, G. Stasińska, & S. K. Gorny, 117
- Ciardullo, R., Durrell, P. R., Laychak, M. B., Herrmann, K. A., Moody, K., Jacoby, G. H., & Feldmeier, J. J. 2004, *ApJ*, 614, 167
- Cristallo, S., Straniero, O., Gallino, R., Piersanti, L., Domínguez, I., & Lederer, M. T. 2009, *ApJ*, 696, 797
- Crockett, N. R., Garnett, D. R., Massey, P., & Jacoby, G. 2006, *ApJ*, 637, 741
- De Robertis, M. M., Dufour, R. J., & Hunt, R. W. 1987, *JRASC*, 81, 195
- Esteban, C., Bresolin, F., Peimbert, M., García-Rojas, J., Peimbert, A., & Mesa-Delgado, A. 2009, *ApJ*, 700, 654
- Freedman, W. L., Madore, B. F., Gibson, B. K., et al. 2001, *ApJ*, 553, 47
- Froese Fischer, C., & Tachiev, G. 2004, *Atomic Data and Nuclear Data Tables*, 87, 1
- Froese Fischer, C., Tachiev, G., & Irimia, A. 2006, *Atomic Data and Nuclear Data Tables*, 92, 607
- Galavis, M. E., Mendoza, C., & Zeppen, C. J. 1995, *A&AS*, 111, 347
- Garnett, D. R. 1992, *AJ*, 103, 1330
- Górny, S. K., Chiappini, C., Stasińska, G., & Cuisinier, F. 2009, *A&A*, 500, 1089
- Haffner, L. M., Dettmar, R., Beckman, J. E., et al. 2009, *Reviews of Modern Physics*, 81, 969
- Henry, R. B. C. 1989, *MNRAS*, 241, 453
- Henry, R. B. C., Kwitter, K. B., & Balick, B. 2004, *AJ*, 127, 2284
- Howard, J. W., Henry, R. B. C., & McCartney, S. 1997, *MNRAS*, 284, 465
- Hudson, C. E., & Bell, K. L. 2005, *A&A*, 430, 725
- Hummer, D. G., & Storey, P. J. 1987, *MNRAS*, 224, 801
- Hunter, I., Brott, I., Langer, N., et al. 2009, *A&A*, 496, 841
- Hunter, I., Brott, I., Lennon, D. J., et al. 2008, *ApJL*, 676, L29
- Izotov, Y. I., Stasińska, G., Meynet, G., Guseva, N. G., & Thuan, T. X. 2006, *A&A*, 448, 955
- Kashikawa, N., Aoki, K., Asai, R., et al. 2002, *PASJ*, 54, 819
- Kaufman, V., & Sugar, J. 1986, *Journal of Physical and Chemical Reference Data*, 15, 321
- Kennicutt, Jr., R. C., Stetson, P. B., Saha, A., et al. 1998, *ApJ*, 498, 181
- Kingsburgh, R. L., & Barlow, M. J. 1994, *MNRAS*, 271, 257
- Kniazev, A. Y., Pustilnik, S. A., & Zucker, D. B. 2008, *MNRAS*, 384, 1045
- Kwitter, K. B., & Aller, L. H. 1981, *MNRAS*, 195, 939
- Leisy, P., & Dennefeld, M. 1996, *A&AS*, 116, 95
- . 2006, *A&A*, 456, 451
- Lodders, K. 2003, *ApJ*, 591, 1220
- Maciel, W. J., & Quireza, C. 1999, *A&A*, 345, 629
- Maeder, A., & Meynet, G. 2000, *ARAA*, 38, 143
- Magrini, L., Cardwell, A., Corradi, R. L. M., Mampaso, A., & Perinotto, M. 2001, *A&A*, 367, 498
- Magrini, L., Leisy, P., Corradi, R. L. M., Perinotto, M., Mampaso, A., & Vílchez, J. M. 2005, *A&A*, 443, 115
- Magrini, L., Stanghellini, L., & Villaver, E. 2009, *ApJ*, 696, 729
- Magrini, L., Vílchez, J. M., Mampaso, A., Corradi, R. L. M., & Leisy, P. 2007, *A&A*, 470, 865
- Marigo, P. 2001, *A&A*, 370, 194
- Marigo, P., Bernard-Salas, J., Pottasch, S. R., Tielens, A. G. G. M., & Wesselius, P. R. 2003, *A&A*, 409, 619
- Marigo, P., Girardi, L., Weiss, A., Groenewegen, M. A. T., & Chiosi, C. 2004, *A&A*, 423, 995
- Massey, P., Armandroff, T. E., Pyke, R., Patel, K., & Wilson, C. D. 1995, *AJ*, 110, 2715
- Massey, P., Bianchi, L., Hutchings, J. B., & Stecher, T. P. 1996, *ApJ*, 469, 629
- McLaughlin, B. M., & Bell, K. L. 2000, *Journal of Physics B Atomic Molecular Physics*, 33, 597
- Mendoza, C. 1983, in *IAU Symposium*, Vol. 103, *Planetary Nebulae*, ed. D. R. Flower, 143
- Oke, J. B., Cohen, J. G., Carr, M., et al. 1995, *PASP*, 107, 375
- Peña, M., Stasińska, G., & Richer, M. G. 2007, *A&A*, 476, 745
- Peimbert, M. 1978, in *IAU Symposium*, Vol. 76, *Planetary Nebulae*, ed. Y. Terzian, 215–223
- Pérez-Montero, E., Hägele, G. F., Contini, T., & Díaz, A. I. 2007, *MNRAS*, 381, 125
- Porter, R. L., Ferland, G. J., & MacAdam, K. B. 2007, *ApJ*, 657, 327
- Prantzos, N., & Boissier, S. 2000, *MNRAS*, 313, 338
- Press, W. H., Teukolsky, S. A., Vetterling, W. T., & Flannery, B. P. 1992, *Numerical recipes in FORTRAN. The art of scientific computing* (Cambridge University Press)
- Ramsbottom, C. A., Bell, K. L., & Stafford, R. P. 1996, *Atomic Data and Nuclear Data Tables*, 63, 57
- Richer, M. G. 1993, *ApJ*, 415, 240
- Richer, M. G., & McCall, M. L. 2007, *ApJ*, 658, 328
- . 2008, *ApJ*, 684, 1190
- Rosolowsky, E., & Simon, J. D. 2008, *ApJ*, 675, 1213
- Rubin, R. H., Simpson, J. P., Colgan, S. W. J., et al. 2008, *MNRAS*, 387, 45
- Scowcroft, V., Bersier, D., Mould, J. R., & Wood, P. R. 2009, *MNRAS*, 396, 1287
- Seaton, M. J. 1979, *MNRAS*, 187, 73P
- Shaw, R. A., & Dufour, R. J. 1995, *PASP*, 107, 896
- Stanghellini, L., Guerrero, M. A., Cunha, K., Machado, A., & Villaver, E. 2006, *ApJ*, 651, 898
- Stasińska, G. 2005, *A&A*, 434, 507
- Stasińska, G. 2008, in *EAS Publications Series*, Vol. 32, *EAS Publications Series*, ed. C. Charbonnel & J.-P. Zahn, 173–185
- Stasińska, G., Richer, M. G., & McCall, M. L. 1998, *A&A*, 336, 667
- Tayal, S. S. 2007, *ApJS*, 171, 331
- Tayal, S. S., & Gupta, G. P. 1999, *ApJ*, 526, 544

- Torres-Peimbert, S., & Peimbert, M. 1997, in IAU Symposium, Vol. 180, Planetary Nebulae, ed. H. J. Habing & H. J. G. L. M. Lamers, 175
- U, V., Urbaneja, M. A., Kudritzki, R.-P., Jacobs, B. A., Bresolin, F., & Przybilla, N. 2009, *ApJ*, 704, 1120
- Urbaneja, M. A., Herrero, A., Kudritzki, R.-P., Najarro, F., Smartt, S. J., Puls, J., Lennon, D. J., & Corral, L. J. 2005, *ApJ*, 635, 311
- van Dokkum, P. G. 2001, *PASP*, 113, 1420
- Vílchez, J. M., Pagel, B. E. J., Díaz, A. I., Terlevich, E., & Edmunds, M. G. 1988, *MNRAS*, 235, 633
- Wang, W., & Liu, X.-W. 2008, *MNRAS*, 389, L33
- Willner, S. P., & Nelson-Patel, K. 2002, *ApJ*, 568, 679